

4-23-2019

Curie Temperature Enhancement and Cation Ordering in Titanomagnetites: Evidence From Magnetic Properties, XMCD, and Mössbauer Spectroscopy

Julie A. Bowles

University of Wisconsin-Milwaukee, bowlesj@uwm.edu

S.-C. L. L. Lappe

University of Wisconsin-Milwaukee

Mike J. Jackson

University of Minnesota - Twin Cities, jacks057@umn.edu

E. Arenholz

Lawrence Berkeley National Laboratory

G. van der Laan

Diamond Light Source

Follow this and additional works at: https://dc.uwm.edu/geosci_facart

Recommended Citation

Bowles, J. A., Lappe, S.-C. L. L., Jackson, M. J., Arenholz, E., & van der Laan, G. (2019). Curie temperature enhancement and cation ordering in titanomagnetites: Evidence from magnetic properties, XMCD, and Mössbauer spectroscopy. *Geochemistry, Geophysics, Geosystems*, 20, 2272–2289. <https://doi.org/10.1029/2019GC008217>

This Article is brought to you for free and open access by UWM Digital Commons. It has been accepted for inclusion in Geosciences Faculty Articles by an authorized administrator of UWM Digital Commons. For more information, please contact scholarlycommunicationteam-group@uwm.edu.

Geochemistry, Geophysics, Geosystems

RESEARCH ARTICLE

10.1029/2019GC008217

Special Section:

Magnetism in the Geosciences
- Advances and Perspectives

Key Points:

- Synthetic titanomagnetite Curie temperatures increase when annealed at 325–400 degrees C and decrease when rapidly cooled from ~600 degrees C
- XMCD, Mossbauer, and magnetic data suggest the cause is vacancy-enhanced nanoscale chemical clustering
- Vacancies and Mg cations are accommodated on octahedral sites; Al cations are split between octahedral and tetrahedral sites

Supporting Information:

- Supporting Information S1
- Table S1
- Table S2
- Table S3

Correspondence to:

J. A. Bowles,
bowlesj@uwm.edu

Citation:

Bowles, J. A., Lappe, S.-C. L. L., Jackson, M. J., Arenholz, E., & van der Laan, G. (2019). Curie temperature enhancement and cation ordering in titanomagnetites: Evidence from magnetic properties, XMCD, and Mössbauer spectroscopy. *Geochemistry, Geophysics, Geosystems*, 20, 2272–2289. <https://doi.org/10.1029/2019GC008217>

Received 23 JAN 2019

Accepted 21 MAR 2019

Accepted article online 23 APR 2019

Published online 15 MAY 2019

Curie Temperature Enhancement and Cation Ordering in Titanomagnetites: Evidence From Magnetic Properties, XMCD, and Mössbauer Spectroscopy

J. A. Bowles¹ , S.-C. L. L. Lappe^{1,2}, M. J. Jackson³ , E. Arenholz⁴, and G. van der Laan⁵ 

¹Department of Geosciences, University of Wisconsin-Milwaukee, Milwaukee, WI, USA, ²Now at Institute of Crystallography, RWTH Aachen University, Aachen, Germany, ³Institute for Rock Magnetism, Department of Earth Sciences, University of Minnesota, Twin Cities, Minneapolis, MN, USA, ⁴Advanced Light Source, Lawrence Berkeley National Laboratory, Berkeley, CA, USA, ⁵Magnetic Spectroscopy Group, Diamond Light Source, Didcot, UK

Abstract Previous work has documented time- and temperature-dependent variations in the Curie temperature (T_c) of natural titanomagnetites, independent of any changes in sample composition. To better understand the atomic-scale processes responsible for these variations, we have generated a set of synthetic titanomagnetites with a range of Ti, Mg, and Al substitution; a subset of samples was additionally oxidized at low temperature (150 °C). Samples were annealed at temperatures between 325 and 400 °C for up to 1,000 hr and characterized in terms of magnetic properties; Fe valence and site occupancy were constrained by X-ray magnetic circular dichroism (XMCD) and Mössbauer spectroscopy. Annealing results in large (up to ~100 °C) changes in T_c , but Mössbauer, XMCD, and saturation magnetization data all demonstrate that intersite reordering of $\text{Fe}^{2+}/\text{Fe}^{3+}$ does not play a role in the observed T_c changes. Rather, the data are consistent with vacancy-enhanced nanoscale chemical clustering within the octahedral sublattice. This clustering may be a precursor to chemical unmixing at temperatures below the titanomagnetite binary solvus. Additionally, the data strongly support a model where cation vacancies are predominantly situated on octahedral sites, Mg substitution is largely accommodated on octahedral sites, and Al substitution is split between the two sites.

Plain Language Summary Magnetization acquired by the iron-titanium oxide mineral titanomagnetite (frequently found in volcanic rocks) provides a vital source of information about geomagnetic field history and tectonic plate motions. Yet, there are aspects of titanomagnetite's magnetism that remain poorly understood, particularly concerning the arrangement of metal cations (Fe^{2+} , Fe^{3+} , Ti^{4+} , etc.) in the crystal structure, how the arrangement changes with temperature, and resulting changes in magnetic properties. Recent findings demonstrate that naturally occurring titanomagnetites exhibit dramatic changes in certain magnetic properties when subjected to moderate temperatures (300–500 °C). These changes can influence the outcome of laboratory procedures designed to recover valuable information about Earth's magnetic field. Here, we created synthetic titanomagnetite and used techniques that provide information on the arrangement of cations within the crystal structure. Titanomagnetite has two distinct types of “sites” in which metal cations can be situated. One way to produce the observed magnetic variations is to change the distribution of iron cations *between* these two sites. However, this work demonstrates that the observed magnetic property variations are *not* related to this type of rearrangement of iron cations. Instead, it appears to be related to oxidation and may result from a rearrangement of cations *within* one of the crystal sites.

1. Introduction

Titanomagnetites (TMs) are some of the most common natural magnetic minerals. Many paleomagnetic studies rely on thermoremanent magnetization held by TM to provide information on a host of geologic processes including geomagnetic field variations, geodynamo evolution, and tectonic plate reconstructions. Proper interpretation of these data requires a thorough understanding of TM mineral magnetism. However, recent work has shown that the Curie temperatures (T_c) of many common TMs are strongly dependent on thermal history in a way that was unexpected and which affects the blocking temperature spectrum (Bowles et al., 2013; Jackson & Bowles, 2014, 2018), thus affecting remanence acquisition and retention (Bowles

et al., 2015; Bowles & Jackson, 2016). Understanding the fundamental underlying mechanism is critical for proper assessment of thermoremanent magnetization acquisition and removal both in nature and in standard laboratory protocols.

TMs constitute a solid solution series, $\text{Fe}_{3-x}\text{Ti}_x\text{O}_4$ ($0 \leq x \leq 1$), with end-members magnetite ($x = 0$) and ulvöspinel ($x = 1$). They crystallize in the cubic spinel structure, which consists of close-packed oxygen anions with the metal cations occupying tetrahedral (A) and octahedral (B) interstices. Below T_c , a net spontaneous magnetization arises due to antiferromagnetic coupling between the A and B sublattices (Néel, 1948, 1955), and magnetic properties strongly depend on the arrangement of cations within and between the different lattice sites (Kakol et al., 1991; Lattard et al., 2006; Stephenson, 1972a, 1972b). It is therefore conceivable that the observed variations in T_c may reflect a reordering of the metal cations.

For any two-cation spinel ($X^{2+}Y^{3+}_2\text{O}_4$) two extreme cation arrangements are possible. The normal arrangement is $X^{2+}[Y^{3+}_2]\text{O}_4$, while the inverse arrangement is $Y^{3+}[X^{2+}Y^{3+}]\text{O}_4$, where square brackets denote octahedral site occupancy. Intermediate arrangements of cations can be represented by an inversion or distribution parameter, ϵ , such that $X^{2+}_{1-\epsilon}Y^{3+}_\epsilon[X^{2+}_\epsilon Y^{3+}_{2-\epsilon}]\text{O}_4$, ϵ ranges from 0 for normal ordering through $2/3$ for a random (disordered) distribution, to 1 for the perfect inverse arrangement. The equilibrium value of ϵ is temperature dependent, with higher temperatures promoting more disorder. For TMs with the paired substitution of $\text{Ti}^{4+} + \text{Fe}^{2+} \leftrightarrow 2\text{Fe}^{3+}$, describing cation site occupancy becomes more complicated, requiring two distribution parameters and one composition parameter (e.g., O'Neill & Navrotsky, 1984). However, it is generally agreed that Ti^{4+} is restricted to the octahedral site and that increasing Ti content requires a redistribution of Fe^{2+} and Fe^{3+} between sites (Pearce et al., 2010).

A variety of models have been proposed to describe the room temperature equilibrium variations in cation ordering within the TM series (Akimoto, 1954; Chevallier et al., 1955; Kakol et al., 1991; Néel, 1955; O'Reilly & Banerjee, 1965). These range from the relatively ordered model of Néel (1955), where the Ti substitution only affects octahedral-site cations for compositions $x \leq 0.5$, to the more disordered model of Akimoto (1954) where both tetrahedral and octahedral-site Fe^{3+} are replaced at the same rate. Current models based on saturation magnetization, Mössbauer spectra, and X-ray magnetic circular dichroism (XMCD) strongly suggest something intermediate between these end-members (e.g., Hamdeh et al., 1999; Kakol et al., 1991; Lilova et al., 2012; Pearce et al., 2010).

1.1. Time- and Temperature-Dependent Changes in TM Curie Temperature

Reordering of metal cations with changing Ti content influences T_c , as well as saturation magnetization (M_s), and one would expect that reordering at constant composition would also influence magnetic properties. Previously observed changes in T_c at constant composition have been explained in the context of thermally activated crystal-chemical reordering within the TM spinel structure. In natural TMs, T_c varies by up to 150 °C with isothermal annealing at moderate temperatures ($T_a \approx 300\text{--}450$ °C) in the sense that longer anneal times (t_a) produce higher T_c . In this framework, a higher degree of ordering is associated with a higher T_c , the equilibrium degree of ordering is inversely temperature dependent, and the rate of ordering is typically slower at lower temperatures. We refer the reader to Bowles et al. (2013) and Jackson and Bowles (2014, 2018) for details of previous observations and a theoretical explanation of the reordering phenomenon. We briefly summarize the key points here.

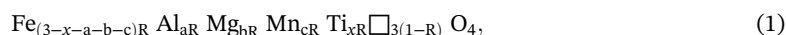
As a sample cools from high temperature, the TM becomes progressively more ordered until it reaches a closure temperature, T_{close} , where the rate of ordering becomes negligible, and the order degree at T_{close} is locked in as the sample continues to cool. T_{close} is rate dependent, so faster cooling will result in more disordered final states and lower T_c (see Figure 6 in Bowles et al., 2013). If a rapidly cooled, relatively disordered sample is then annealed at moderate temperatures, the TM will become progressively more ordered until reaching the equilibrium degree of order at T_a . If this annealed sample is then heated rapidly in the lab during a thermomagnetic experiment, the sample will disorder at $T > T_{\text{close}}$. When cooled at this same rapid rate, a lower degree of order and lower T_c is locked in. This results in thermomagnetic data where T_c measured on warming is higher, reflecting the prior thermal history and relatively ordered state; T_c measured on cooling is lower, reflecting the rapid cooling and relatively disordered state. For heating and cooling on these laboratory timescales ($\sim 8\text{--}12$ °C/min), we find that T_{close} is approximately 475–500 °C.

Previous work has shown that natural samples can be repeatedly ordered and disordered (with accompanying changes in T_c) with little to no accompanying change in bulk chemistry (Bowles et al., 2013; Jackson & Bowles, 2014, 2018). The key question revolves around understanding the atomic-scale changes that produce this phenomenon. Similar T_c changes have been observed in magnesioferrite and are convincingly attributed to intersite reordering of iron cations (Harrison & Putnis, 1999a, 1999b), but this does not seem to be an entirely satisfactory explanation for the TM changes. Limited M_s data do not appear to change significantly with annealing (Bowles et al., 2013; Jackson & Bowles, 2018), suggesting that intersite $\text{Fe}^{2+}/\text{Fe}^{3+}$ reordering is not the dominant mechanism. Jackson and Bowles (2018) explore the idea that oxidation state or degree of nonstoichiometry plays a key role. Samples annealed under inert or reducing conditions exhibit smaller changes in T_c than samples annealed in air. Other work has also suggested a link between cation vacancies and cation reordering (e.g., Lattard et al., 2006; Moskowitz, 1987; Wanamaker & Moskowitz, 1994). Jackson and Bowles (2018) also find that large increases in T_c seem to be roughly limited to temperatures below the TM binary solvus over the compositional range studied ($0.25 < x < 0.6$), leading to the speculation that nanophase chemical unmixing/rehomogenization plays a role. They suggest a hybrid model with nanoscale chemical clustering and octahedral intrasite cation redistribution, as in the thermodynamic models of magnesioferrite-quandilite of Harrison et al. (2013).

In this paper we use synthetic TMs of controlled composition to further constrain the atomic-scale processes responsible for the time- and temperature-dependent variations in T_c . One outstanding question has been whether or not common substitute cations found in almost all natural samples (e.g., Al, Mg, and Mn) are required or play a role. We will show that thermal history controls T_c in the same way as it does for the natural samples, and we find no significant differences between TM samples with or without substitute cations. Use of XMCD and Mössbauer spectroscopy allows us to verify that intersite exchange of $\text{Fe}^{2+}/\text{Fe}^{3+}$ does not play a significant role in the T_c variations and also allows us to place constraints on the site occupancies of Mg, Al, and vacancies in the TM structure. Finally, oxidation experiments further reinforce the notion that vacancies play an important role in the observed T_c variations.

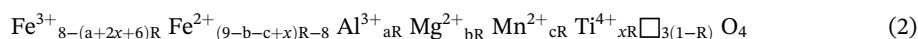
1.2. Generalized Structural Formula for Variably Substituted and Cation-Deficient TMs

To facilitate discussion below, and to calculate T_c and M_s trends, we need a generalized chemical formula for variably cation-deficient impure TMs. From (O'Reilly, 1984, section 2.1.1),



where \square is a cation vacancy and R is related to stoichiometry, defined such that $3R$ equals the total number of cations per four anions (where $1 \geq R \geq 8/[9 + x - b - c]$). R is related to the commonly used cation-deficiency parameters δ and z by $(1 - R) = \delta = z/3$.

Charge balance gives the cation-specific formula



To specify the distribution of cations into the tetrahedral and octahedral sites, we assume that all Ti and vacancies are octahedrally coordinated (e.g., Pearce et al., 2006; Wechsler et al., 1984), and that the remaining ions are partitioned between sites.

Because we decrease both Fe and Ti when substituting the other cations (see section 2.1), we modify these formulas as needed to calculate trends with increasing impurity substitution. See supporting information for details.

2. Methods

2.1. Sample Synthesis

TM samples were synthesized in an approach similar to that outlined in Pearce et al. (2010). Stoichiometric mixtures of Fe_2O_3 , TiO_2 , Fe^0 , Al_2O_3 , MgO , and MnO were ground together under acetone for ~1 hr. The mixed powder was filled into Ag capsules and placed into evacuated quartz tubes. Samples were heated to 900 °C over 20 hr, kept at this temperature for 12 days, and then cooled to room temperature over 20 hr.

Table 1
Intended and Measured Composition of Synthetic Samples on Cation Basis

Sample ID	Intended composition						Measured composition						
	x'	Fe	Ti	Al	Mg	Mn	x'	Fe	Ti	Al	Mg	Mn	T_c
b11_25M	0.25	2.60	0.24	0.08	0.08	0	0.25	2.61	0.24	0.07	0.09	0.00	401
b12_25M	0.25	2.60	0.24	0.08	0.08	0	0.26	2.58	0.25	0.08	0.09	0.00	410
b12_30M	0.29	2.56	0.28	0.08	0.08	0	0.28	2.57	0.27	0.08	0.09	0.00	383
b11_30MMn	0.29	2.55	0.28	0.08	0.08	0.01	0.26	2.51	0.24	0.15	0.08	0.01	376
b13_35P	0.35	2.65	0.35	0	0	0	0.33	2.67	0.33	0.00	0.00	0.00	375
b13_35L	0.35	2.54	0.34	0.06	0.06	0	0.33	2.56	0.32	0.06	0.06	0.00	363
b11_35M	0.34	2.51	0.33	0.08	0.08	0	0.35	2.51	0.34	0.07	0.08	0.00	336
b12_35M	0.34	2.51	0.33	0.08	0.08	0	0.33	2.52	0.32	0.08	0.08	0.00	350
b13_35H	0.34	2.44	0.32	0.12	0.12	0	0.32	2.45	0.30	0.13	0.12	0.00	343
b14_40P	0.40	2.60	0.40	0	0	0	0.38	2.61	0.38	0.01	0.00	0.00	340
b14_50L	0.49	2.40	0.48	0.06	0.06	0	0.47	2.43	0.46	0.06	0.06	0.00	249
b14_60P	0.60	2.40	0.60	0	0	0	0.57	2.44	0.57	0.00	0.00	0.00	180

Note. Sample naming convention: bxx represents the batch number; next two numbers are the approximate TM content; and the final letter is related to the purity of the TM, P for “pure,” L for “low” amounts of Mg and Al substitution, M for “medium,” and H for “high.” x' is the projection of the TM x compositional parameter onto the magnetite-ulvöspinel join (after Evans et al., 2006). For pure TM, $x = x'$. Measured compositions determined by electron microprobe analysis. T_c is determined from the measured $k(T)$ cooling curve. TM = Titanomagnetite.

To ensure a uniform and reproducible initial state for all the samples, they were equilibrated at 450 °C for 100 hr, heated to 650 °C ($>T_{\text{close}}$) for 1 hr, and then rapidly cooled to room temperature. The quartz tubes were opened within a portable glove box under N₂ atmosphere. Portions of each sample were wrapped in aluminum foil and placed in evacuated quartz tubes for annealing experiments designed to put the samples in various states of order.

Intended and actual compositions are given in Table 1. Prepared compositions include pure TM ($x = 0.35, 0.40, 0.60$) with only Fe and Ti cations, as well as a suite of samples with Al and Mg impurities. For these latter samples, the nominal TM composition is given by x' (Evans et al., 2006), the projection of the TM x compositional parameter onto the magnetite-ulvöspinel join: $x' = \text{Ti}/(\text{Ti} + \text{Fe}^{3+}/2)$. The amount of Al and Mg impurities are $a = b = 0.06$ cations per formula unit (cpfu) (“low”), 0.08 cpfu (“medium”), or 0.12 cpfu (“high”). One sample also included a small amount of Mn ($c = 0.01$). When making the impurity substitutions, we adjusted both Fe and Ti to maintain an approximately constant Fe:Ti ratio.

2.2. Annealing and Oxidation Experiments

Sample splits were annealed under vacuum at temperatures from 325 to 400 °C for periods of 10 to 1,000 hr. Unlike the serial treatment/measurement experiments documented in, for example, Bowles et al. (2013), where each sample was subjected to many annealing experiments and thermomagnetic runs, the samples in this study were divided into parallel splits, each of which was only used for a single annealing experiment (one temperature and time) and one $k(T)$ thermomagnetic susceptibility run. Compared to most of the prior bulk rock samples, our concentrated TM powders were more susceptible to oxidation when exposed to multiple $k(T)$ runs, even under Ar atmosphere.

To examine the possible role of nonstoichiometry, selected samples were oxidized at low temperature prior to annealing. These samples were first ground using a mortar and pestle and then heated in air at 150 °C for 110.5 hr. The resulting product is interpreted to have a surface oxidation to titanomaghemite (section 3.2.2). After oxidation, samples were contained in silver foil, sealed in evacuated quartz tubes, and annealed for 100 hr at either 350 or 375 °C. One sample (b11_30MMn) was additionally annealed for 10 and 1,000 hr.

After annealing (with or without prior surface oxidation), $k(T)$ was measured at a rate of ~ 12 °C/min. We will refer to the state after this relatively rapid cooling as the quenched state. A complete list of samples and treatments is available in supporting information Table S2.

2.3. Sample Characterization

Samples were characterized in terms of their composition and magnetic properties using X-ray diffraction (XRD), electron microprobe, low-field susceptibility versus temperature, and high-field measurements.

2.3.1. Compositional Characterization

Powder XRD experiments were conducted at University of Wisconsin-Milwaukee (UWM) on a Bruker D8 Focus XRD system at room temperature (Cu K α radiation, 4 s per 0.01° 2 θ , 2–60° range, Sol-X energy dispersive detector). Quantitative electron microprobe data were collected at the University of Wisconsin-Madison Department of Geosciences with a CAMECA SX51 or SXFive FE utilizing Probe for EPMA software (Donovan et al., 2015). Operating conditions were 15 kV and either 30 or 20 nA, with a focused beam, except for the SXFive FE which had a slightly defocused (nominal 1 micron) beam. Backgrounds were determined either by two off-peak settings or by the Mean Atomic Number method (Donovan & Tingle, 1996). The matrix correction used was the Armstrong/Love Scott algorithm (Armstrong, 1988). Standards used were a combination of both natural minerals (Smithsonian Microbeam standards) and synthetic crystals. Fe²⁺ and Fe³⁺ were calculated assuming stoichiometry and three cations per four oxygen (Droop, 1987). Sample average compositions were determined by analyzing multiple grains and retaining any analyses where oxide totals were between 98.5% and 101.5%. We note that this approach is technically incorrect for oxidized samples that may have fewer than three cations per formula unit. However, measurements were mostly made in grain centers and did not appear to have anomalously low totals. Microprobe data may therefore not fully reflect the surface oxidized composition.

2.3.2. Magnetic Characterization

Curie temperatures were determined from $k(T)$ thermomagnetic susceptibility runs measured at UWM using an AGICO MFK1-FA MultiFunction Kappabridge with CS4 furnace attachment. Experiments were conducted under flowing Ar in an AC field with amplitude of 200 A/m, a frequency of 976 Hz, and at a temperature sweep rate of ~12 °C/min. $k(T)$ was measured while warming to and cooling from a peak temperature of 600–650 °C.

At the Institute for Rock Magnetism, low-temperature (25–300 K at 25-K intervals) magnetic hysteresis measurements were made on a Princeton Measurements vibrating-sample magnetometer (VSM, MicroMag model 3900), equipped with a flow-through helium cryostat, using a peak field of 1 T. Loops were processed using the methods of Jackson and Solheid (2010) to calculate the temperature-dependent saturation magnetization, $M_s(T)$; saturation remanence, $M_{rs}(T)$; coercivity, $B_c(T)$; and remanent-hysteretic coercivity, $B_{rh}(T)$. For a subset of samples, M_s was instead determined by measuring hysteresis at 300 and 20 K on a Quantum Designs Magnetic Property Measurement System, using a peak field of 2.5 T.

2.4. X-Ray Absorption Spectroscopy and XMCD

XMCD uses circularly polarized X-rays to probe the electronic and magnetic structure of a material (e.g., Patrick et al., 2002). In ferromagnetic and ferrimagnetic materials, X-ray absorption spectroscopy (XAS) is dichroic with respect to the X-ray polarization, and the XMCD spectrum is defined as the difference between the left- and right-circularly polarized XAS spectra (supporting information Figure S1a). For TMs, XMCD can provide information on Fe site occupancy and valence state (Pearce et al., 2010).

Fe XAS spectra at the Fe $L_{2,3}$ edges were collected at the Advanced Light Source (ALS) at Berkeley National Lab using the eight-pole magnet end station on beamline 4.0.2 (Arenholz & Prestemon, 2005; Young et al., 2001). XAS was measured in total electron yield detection, which is surface-sensitive (sampling depth of 3–5 nm; van der Laan & Figuerao, 2014). Therefore, to avoid surface oxidation, sample preparation at UWM was conducted within a nitrogen-filled glove box. Samples were removed from quartz tubes and briefly ground using mortar and pestle to expose a fresh surface. Powders were attached to the sample holder using carbon tape. The holder was then enclosed in an air-tight glass jar before removal from the N₂ environment. At the beamline, the sample holder was removed from its N₂ environment immediately prior to insertion into the end station airlock. The samples were exposed to air for at least several tens of seconds during this procedure.

Measurements were made at room temperature in fields of +0.5 T and – 0.5 T (to obtain the oppositely polarized X-ray spectra). For each sample, two to three separate sets of spectra were obtained at slightly different locations within the sample surface to verify reproducibility and sample homogeneity. XAS spectra were normalized to the incident beam intensity before obtaining the difference spectra (i.e., the XMCD).

Experimental XMCD spectra were fit with a set of calculated component spectra (supporting information Figure S1b) for each of the four sites (tetrahedral and octahedral Fe²⁺ and Fe³⁺). Component spectra

were calculated as described in van der Laan and Thole (1991). The cubic crystal-field parameter was $10Dq = 1.4$ eV for the octahedral sites and -0.7 eV for the tetrahedral sites. Calculated component spectra were convolved with a Gaussian of $\sigma = 0.2$ eV to account for the instrumental broadening. These component spectra were then fit to the measured spectra using a Nelder–Mead simplex approach (as outlined in Lagarias et al., 1998, and implemented by Matlab™) which penalized mismatch in the four major peak heights in the L_3 edge.

Mg K-edge XAS spectra were collected to provide information on the site occupancy of substituted Mg cations. Spectra were collected at Argonne National Labs on beamline 4-ID-C of the Advanced Photon Source. The Mg data were collected on a previous set of synthetic samples (Lappe et al., 2014), the details of which are not reported here, but which were prepared as described in section 2.1. The two measured compositions ($\text{Fe}_{2.56}\text{Ti}_{0.28}\text{Al}_{0.00}\text{Mg}_{0.16}\text{O}_4$ and $\text{Fe}_{2.58}\text{Ti}_{0.26}\text{Al}_{0.08}\text{Mg}_{0.08}\text{O}_4$) were prepared in a range of anneal states.

2.5. Mössbauer Spectroscopy

Mössbauer specimens were prepared by dispersing ~10 mg of powdered TM in roughly 50 mg of powdered sugar and spreading the mixture within a nylon ring between two layers of Kapton tape, thereby forming a disk approximately 1 mm thick and 1 cm in diameter. Spectra were measured using a conventional constant-acceleration spectrometer (Web Research) in transmission geometry with a $^{57}\text{Co}/\text{Rh}$ source. Isomer shifts (ISs) and velocity scale were calibrated using an α -Fe foil standard at room temperature. Samples were measured at room temperature and at 4.2 K, in fields of 0 and 5.5 T, applied perpendicular to the gamma-ray beam. Spectra were fit using custom software to obtain estimates for the hyperfine field (B_{HF}), IS, quadrupole splitting (QS), linewidth (Γ), and relative area (A) for each magnetically ordered sextet subspectrum, as well as the IS, QS, Γ , and A parameters for paramagnetic doublet components. Initial four-sextet fits were obtained interactively and were then optimized using a conjugate-gradient algorithm (Press et al., 1986). Area ratios for the six peaks of each sextet were constrained in the fitting to 3:2:1:1:2:3 for zero-field (ZF) and 3:4:1:1:4:3 for transverse in-field (IF) data (Gütlich et al., 2011). ZF and IF spectra were fit simultaneously, with appropriate field shifts for the tetrahedral and octahedral IF sextets, to produce models consistent with both data sets.

In room temperature Mössbauer spectra without an applied field, previous studies have shown that separation of the TM subspectra becomes difficult for $x > 0.2$ because of broad line widths and strong overlaps (e.g., Hamdeh et al., 1999; Jensen & Shive, 1973; Lilova et al., 2012; Sorescu et al., 2012; Tanaka & Kono, 1987). At room temperature, electron hopping between Fe^{2+} and Fe^{3+} ions in the B sites (and possibly also in the A sites) occurs on timescales shorter than the Mössbauer measurement time, and consequently the Fe^{2+} and Fe^{3+} are blurred together in the Mössbauer spectra, yielding a broadened composite sextet with an average oxidation state of $\text{Fe}^{2.5+}$. Measurements at 4.2 K, where electron hopping is suppressed (e.g., Walz et al., 1997), allow sharper distinction of iron valence states, and the application of a strong field allows clearer resolution of sites by shifting the A-site and B-site subspectra in opposite directions. Because of the dominance of the B sublattice moment and negative A-B exchange interactions, the moments of the B-site cations align with the applied field and those of the A site in the antiparallel direction, effectively decreasing and increasing the B- and A-site hyperfine fields, respectively (e.g., Daniels & Rosencwaig, 1969; Hamdeh et al., 1999; Murad & Cashion, 2004).

Hamdeh et al. (1999) determined the cation site occupancy in their synthetic pure TMs ($a = b = c = 0$) using low-temperature IF Mössbauer data with a 7-T field applied parallel to the gamma rays, by fitting only the pair of peaks with highest positive and negative velocity, which were clearly isolated from the rest of the absorption spectrum and which they interpreted as belonging entirely to the tetrahedral-site Fe^{3+} sextet. The cation distribution can be calculated from the area fraction, f , of this sextet, under the constraint of charge balance and assuming no cation vacancies, no low- T electron hopping, and Ti^{4+} constrained to B sites:

$$\text{Fe}_{f(3-x)}^{3+}\text{Fe}_{1-f(3-x)}^{2+}\left[\text{Fe}_{2(1-x)-f(3-x)}^{3+}\text{Fe}_{x+f(3-x)}^{2+}\text{Ti}_{x}^{4+}\right]\text{O}_{2-4} \quad (3)$$

We apply this method in slightly modified form for determination of the cation distribution in our samples. Following Hamdeh et al. (1999), we assume that the isolated peaks with maximum positive and negative

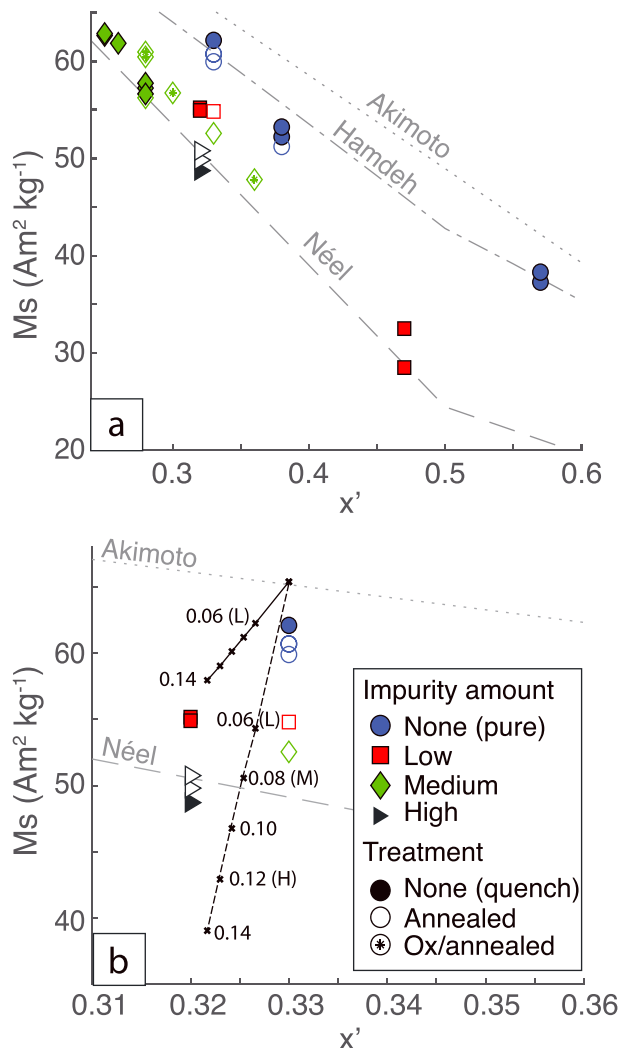


Figure 1. (a) Saturation magnetization at 20–25 K as a function of TM content. Color/shape keyed to relative amount of Mg/Al/Mn impurities. Solid (open) symbols are quenched (annealed). Open symbols with star are oxidized and annealed. For comparison are shown M_s at 0 K predicted by the cation distribution models of Akimoto (1954), Neel-Chevalier (Chevallier et al., 1955; Néel, 1955), and Hamdeh et al. (1999). (b) Zoom into samples with nominal $x' = 0.35$ composition. Black lines are models for Mg and Al substitution where ticks represent $a = b = 0.06$ apfu (“low”), 0.08 (“medium”), 0.10, 0.12 (“high”), and 0.14. Dashed line represents all Mg and Al substitution into the octahedral site. Solid line is random substitution between the two sites. TM = Titanomagnetite.

velocity are entirely attributable to tetrahedral-site Fe^{3+} . The area fraction f of the sextet containing these peaks thus corresponds to the ratio

$${}_{\text{A}}\text{Fe}^{3+}/{}_{\text{tot}}\text{Fe} \equiv f = 3\varepsilon/[(3-x)R(3-a-b-c)], \quad (4)$$

which is sensitive not only to the unknown $\text{Fe}^{2+}/\text{Fe}^{3+}$ inversion (ε) but also to the unknown cation deficiency (R) and the known substitutions (a, b, c).

3. Results

3.1. Compositional Results

Powder XRD measurements show only single-phase TM for all prepared compositions. Electron microprobe data reveal that some samples have a limited number of crystals with Ti-rich ilmenite cores and TM rims. This likely explains why the Fe:Ti ratio in the cubic TM phase is slightly higher than intended for most samples. Summary microprobe data for all as-made samples (no treatment) are provided in Table 1. Additional details, including data on selected annealed and/or oxidized samples, are given in supporting information Table S1. Because most samples were contained in Al foil during annealing, we analyzed five Al-annealed sample splits to assess changes in sample Al content. Three of these were “pure” TMs that started with no Al and thus provide the most straightforward interpretation. Sample b13_35P was annealed for 100 hr at 375 °C, resulting in a significant but highly variable increase in Al (0.07 cpfu average). However, splits of sample b14_40P were annealed for 1,000 hr at 375 °C or for 100 hr at 350 °C, and both show no increase in Al.

3.2. Magnetic Results

3.2.1. Saturation Magnetization

Statistical tests (Jackson & Solheid, 2010) indicate a lack of saturation in the field range up to 1 T, especially for the higher-Ti samples and for measurements at low temperature, so M_s was estimated by approach-to-saturation fits (Fabian, 2006; Jackson & Solheid, 2010). Such fits may still underestimate M_s when samples are far from saturation in the available field range (Fabian, 2006; Jackson & Solheid, 2010). For our synthetic TMs, the temperature dependence for some samples suggests that the calculated M_s values are erroneously low for temperatures below about 100 K; $M_s(T)$ increases on cooling, reaches an apparent maximum near 75–100 K, and then in many cases decreases on further cooling (supporting information Figure S2). We interpret this decrease to be an artifact related to sharply increased coercivity at the “pinning transition” in this temperature interval (Church et al., 2011), causing slower approach to saturation.

Despite this moderate underestimate, M_s values determined at 25 K (Figure 1a) are generally similar to those compiled in previous TM studies (Hunt et al., 1995; Lattard et al., 2006) and are in the range predicted by various cation distribution models. The 1-T VSM results, fit with an approach-to-saturation model, agree well with the 2.5-T Magnetic Property Measurement System results. As expected, the pure TMs have the highest M_s values and fall closest to those predicted by recent cation distribution models suggesting an intermediate degree of order (e.g., Hamdeh et al., 1999). Importantly, there are no obvious or systematic differences between quenched, annealed, or oxidized/annealed samples.

The effects of Al and Mg substitution in TM30 and TM35 are shown more clearly in Figure 1b (see also supporting information Figure S3). Here, we compare the data to two simple model predictions, each using the disordered Akimoto $\text{Fe}^{2+}/\text{Fe}^{3+}$ distribution and involving equal substitutions ($a = b$) ranging from 0 to

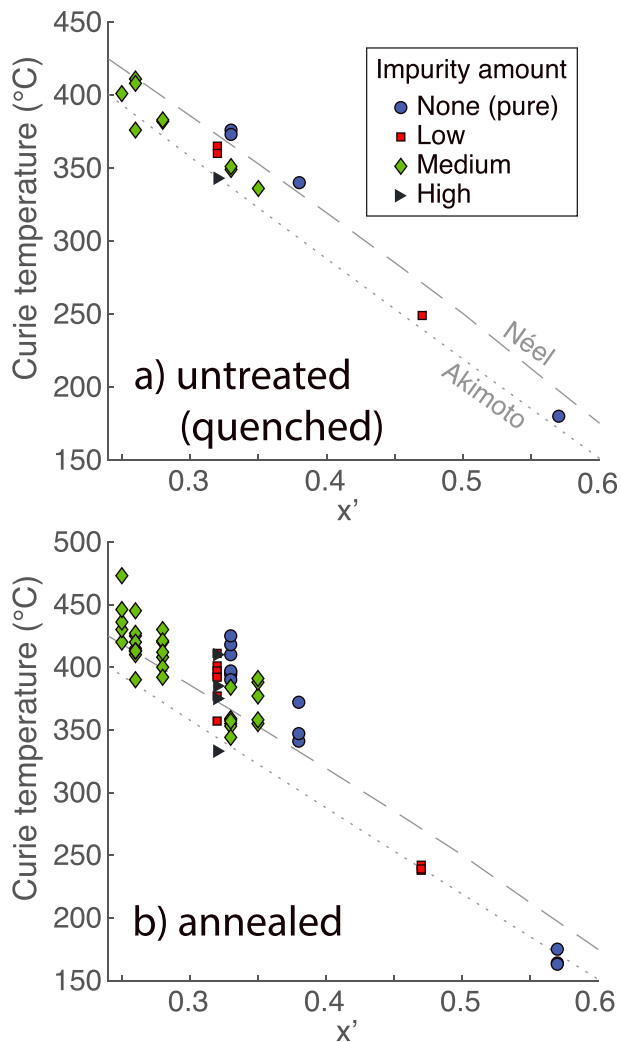


Figure 2. T_c as a function of titanomagnetite composition. (a) Untreated (quenched) samples. T_{c-cool} is plotted to avoid variations associated with thermal history. (b) Annealed samples. T_{c-heat} reflects changes produced by the annealing treatment. For comparison are shown Curie temperatures predicted by the model of Stephenson (1972b) for the cation distribution models of Akimoto (1954) and Néel-Chevalier (Chevallier et al., 1955; Néel, 1955).

with anneal time for a given temperature (Figures 3a and 3b). By contrast, T_{c-cool} decreases slightly (up to ~ 15 °C; Figure 3a). Because T_{c-cool} should not reflect prior thermal history, this suggests that the bulk TM composition has changed during annealing. This is true of samples annealed in either Al or Ag foil, so a possible increase in Al does not explain the T_c decrease. We suggest instead that annealing under vacuum resulted in a slight reduction of the samples, which may not have been perfectly stoichiometric, as indicated by the presence of some ilmenite cores (section 3.1). This would be accompanied by a decrease in T_c , but we acknowledge there may be some other explanation. However, a similar decrease in T_c has been observed in natural samples when annealed in inert nitrogen or graphite (Jackson & Bowles, 2018).

For constant anneal time ($t_a = 100$ hr) at variable anneal temperatures (325–400 °C), ΔT_c is maximized at $T_a = 350$ or 375 °C for most samples. For low degrees of Ti substitution ($0.25 \leq x' \leq \sim 0.4$), there is no systematic variation in behavior with x' . For greater values of x' , ΔT_c decreases with increasing Ti content up to $x' = 0.6$ (the maximum investigated). Synthetic samples that were oxidized prior to annealing produce results similar to the nonoxidized counterparts, but ΔT_c is larger in every case, by up to 59 °C (Figure 4 and supporting information Figure S4).

0.14 cpfu. In one model these cations go entirely into the B site, and in the other they are incorporated randomly (one third into A and two thirds into B). Preferential B-site substitution causes a larger decrease in M_s than random substitution, because in the former, m_A is constant, and all of the decrease applies to m_B , so $m_s = m_B - m_A$ decreases as strongly as possible. The measured M_s values are very consistent with a moderately disordered Fe^{2+}/Fe^{3+} distribution and with substitution of Al and Mg preferentially into the octahedral site (Figure 1b).

3.2.2. Thermomagnetic Results

T_c recorded on heating and cooling for each sample are given in supporting information Table S2. For most samples, the $k(T)$ warming and cooling segments each exhibited a single T_c . For a few of the annealed or oxidized splits, two Curie temperatures were measured on warming. T_c measured on warming (T_{c-heat}) reflects the prior thermal history of the sample, while T_c measured on cooling (T_{c-cool}) is assumed to have the same thermal history for all samples (cooled at 12 °C/min from $T > T_{close}$) and is most reflective of the bulk TM composition. To facilitate comparison of annealing effects across a wide range of TM compositions, we define $\Delta T_c = T_{c-heat} - T_{c-cool}$. This approximately represents the increase in T_c during the anneal treatment compared to the quenched state. When two T_c s are present on warming, we use the higher of the two in this calculation.

For untreated samples (Figure 2a), T_c is approximately linear with Ti content, as represented by x' . With increasing Al, Mg, and Mn substitution, T_c is systematically reduced. For both the pure TMs and the TMs with low impurity substitutions, T_c for $x' < 0.4$ is close to that predicted by Stephenson (1972b) for the more ordered Néel-Chevalier model, but for $x' > 0.45$, T_c is closer to that of the more disordered Akimoto model. As expected, annealed samples have systematically higher T_c , but only for $x' < 0.4$ (Figure 2b). These T_c s are significantly higher (> 50 °C) than predicted for the most ordered of the cation distribution models. For $x' > 0.45$, there is little to no difference in T_c between the quenched and annealed states (< 5 °C).

In untreated samples, we frequently see $T_{c-cool} > T_{c-heat}$, resulting in a negative ΔT_c . We interpret this to represent a sample that cooled faster during the synthesis process than it did during the $k(T)$ measurements, similar to the findings of Lattard et al. (2006). When these untreated samples are annealed, in most cases T_{c-heat} and ΔT_c increase systematically

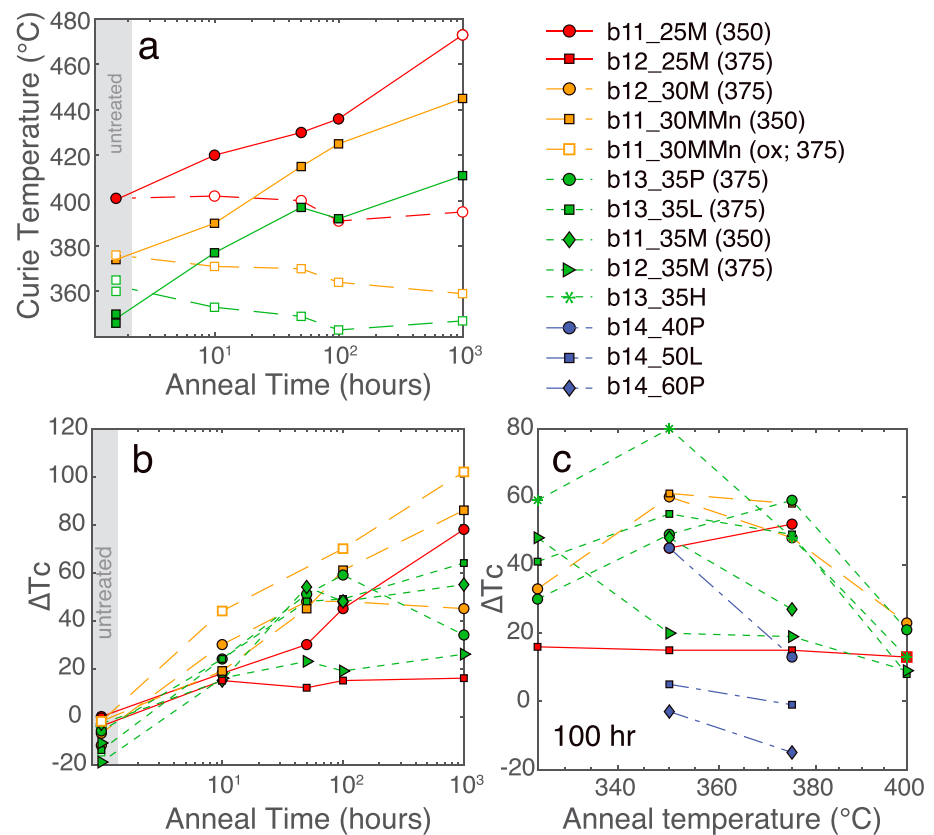


Figure 3. Effects of annealing on Curie temperature. (a) Example T_c data for three samples. T_{c-heat} shown by solid lines, T_{c-cool} by dashed lines. (b) $\Delta T_c = T_{c-heat} - T_{c-cool}$ for all samples annealed at 350 or 375 °C for 10 to 1,000 hr. (c) ΔT_c for all samples annealed for 100 hr at variable temperatures (given in parentheses in key). “ox” indicates sample was oxidized at 150 °C prior to annealing.

Following oxidation (prior to annealing), almost all samples develop two distinct Curie temperatures when measured on heating (supporting information Figure S4). One is close to that of the untreated material, while the second is ~25 °C higher. We interpret this to represent a surface oxidation (likely titanomaghemite) while the interior of the TM grains remains unoxidized. On cooling, the samples display a single T_c

that is intermediate between the two T_c s measured on warming. This may represent homogenization of the sample as it is heated to high temperatures during the $k(T)$ experiment. Repeated $k(T)$ experiments to successively higher temperatures show that this homogenization happens at temperatures between about 300 and 500 °C. After annealing, all oxidized samples have a single T_{c-heat} .

3.3. Site Coordination Results (XAS, XMCD, and Mössbauer)

For simultaneous fitting of the low-temperature Mössbauer ZF and IF spectra, we used the simplest reasonable model, with two octahedral and two tetrahedral sextets to allow for Fe²⁺ and Fe³⁺ ions in each site, with no electron hopping to blur the valence states. The parameters for each sextet were constrained to have equal values in the ZF and IF fitting, with the applied field added to B_{HF} for the tetrahedral sextets and subtracted from B_{HF} for the octahedral sextets. The pure TM40 sample (Figure 5) is representative: the first ZF peak (at about -7.5 mm/s) is split by the applied field into two IF peaks, a sharp one at about -8.5 and a broader one at about -6.5 mm/s. These can be unambiguously ascribed respectively to the tetrahedral and octahedral sites, as done previously

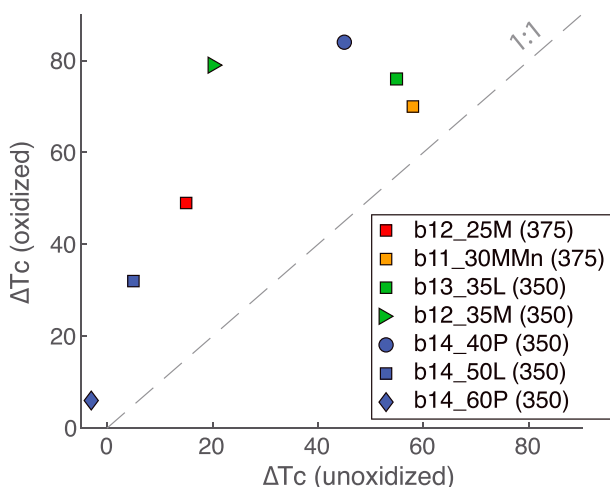


Figure 4. Effects of oxidation on T_c increase during annealing. $\Delta T_c = T_{c-heat} - T_{c-cool}$. Anneal temperature shown in legend. Anneal time = 100 hr.

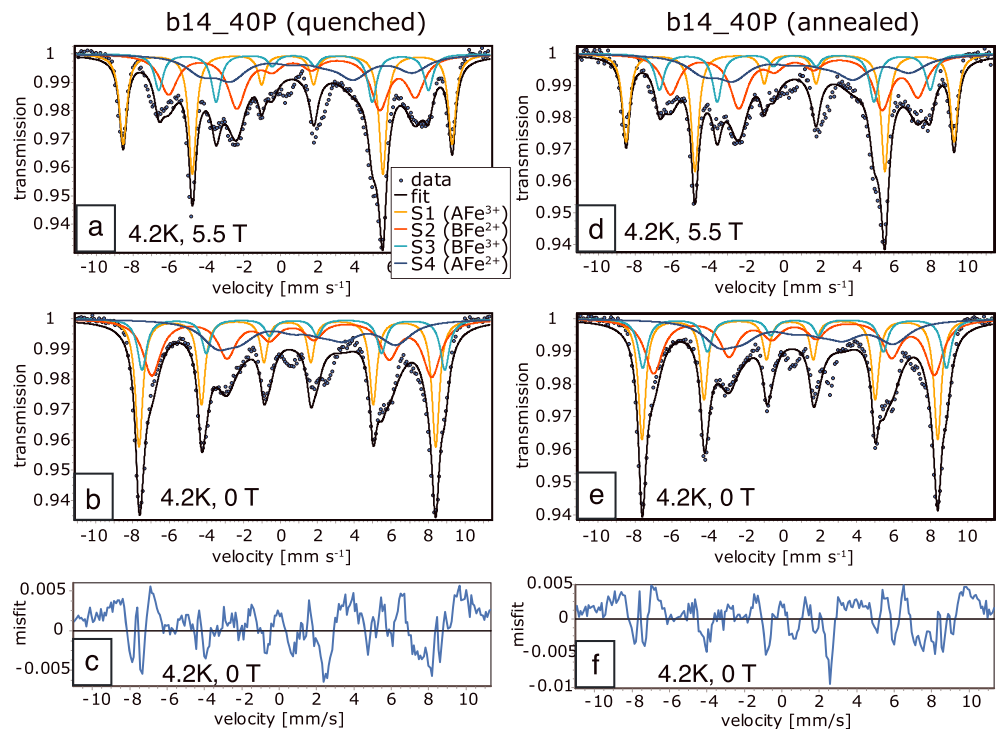


Figure 5. Mössbauer spectra and fits for TM40 measured at 4.2 K. (a, d) Measured in 5.5 T transverse field. (b, e) Measured in zero applied field. (a, b) Sample in quenched state. (d, e) Sample after annealing 1,000 hr at 375 °C. Data shown by individual symbols. Best fit is solid black line. Individual sextets in colored lines, keyed to supporting information Table S4: sextets 1 and 4 correspond to A-site ions, with positive field shifts; sextets 2 and 3 correspond to B-site ions with negative field shifts. Model misfits shown for the zero-field quenched (c) and annealed (f) states.

by Hamdeh et al. (1999), and the tetrahedral-site peak can be fit very well with a relatively narrow Lorentzian having a Γ (full width at half maximum) of 0.5 mm/s and IS of 0.38 mm/s, consistent with a dominantly Fe^{3+} valence. Because the first and last peaks are well isolated in the IF data, the parameters of this sextet are robustly determined, whereas those of the remaining and strongly overlapping sextets are subject to the same nonuniqueness as in ZF data alone.

The major features in the data set are reasonably well reproduced by the simple four-sextet model, and in particular sextet 1 (the A-site ferric sextet) is robustly defined (Figure 5). Much of the fine structure is not accounted for (Figure 5), including a large misfit near 2.5 mm/s, close to a reported absorption peak for ilmenite at low temperature (Shirane et al., 1962). A more complex model is probably not warranted, given the nonuniqueness of the fitting, but since we have identified ilmenite in some grains in our electron microprobe data, we add that to the Mossbauer fits in supporting information Figure S5. It visibly improves the fit in the low velocity range but does not significantly affect the parameters of the major sextets. Sextets 2 and 3 of the four-sextet model can be unambiguously assigned to the octahedral sites because of the negative field shifts, and their ISs respectively suggest Fe^{2+} and Fe^{3+} character. The fourth sextet has a very low hyperfine field and broad linewidths; it is similar to the “C” sextet commonly found in room temperature spectra of intermediate TMs and attributed to Fe^{2+} ions that are not involved in electron hopping (e.g., Hamdeh et al., 1999; Lilova et al., 2012). Although Hamdeh et al. (1999) associates the C sextet with the octahedral site, here the positive field shift associates it with the tetrahedral site. We note, however, that both valence and site are poorly constrained.

Stoichiometry (R) and the Fe inversion parameter (ϵ) can be calculated as follows. For the XMCD data, preliminary calculated Fe^{2+} and Fe^{3+} distributions assume three cations per formula unit and are forced to sum to the total Fe content determined from microprobe analyses. Nonstoichiometry was then calculated using the XMCD experimental $\text{Fe}^{2+}/\text{Fe}^{3+}$ ratio and the known values of a , b , c , and x from microprobe. Vacancies were assigned to octahedral sites, and final Fe cation distributions were adjusted accordingly. ϵ may be found

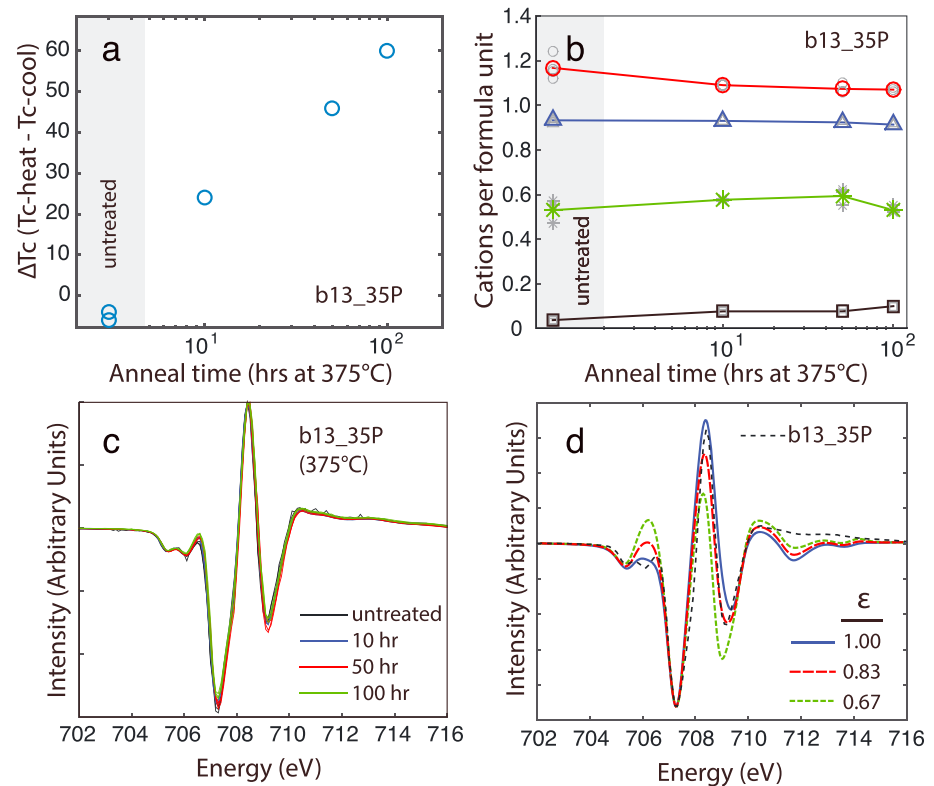


Figure 6. Example XMCD results. (a) T_c variations for sample b13_35P show a systematic and significant increase in T_c with anneal duration at 375 °C. (b) XMCD fit results for same sample show no systematic change in site occupancy with anneal time. Colored symbols are averages of multiple scans. Green stars = $\text{Fe}^{3+}_{\text{oct}}$; blue triangles = $\text{Fe}^{3+}_{\text{tet}}$; red circles = $\text{Fe}^{2+}_{\text{oct}}$; black squares = $\text{Fe}^{2+}_{\text{tet}}$. Light gray symbols from individual scans. (c) All XMCD scans from sample b13_35P. (d) Model XMCD scan profiles for fully ordered ($\epsilon = 1$), random ($\epsilon = 0.67$) and intermediate ($\epsilon = 0.83$) cation distributions. For comparison, data from b13_35P are shown. XMCD = X-ray magnetic circular dichroism.

using equation (4), based on the area fraction of the A-site Fe^{3+} contribution to the XMCD spectra. Because of the nonuniqueness in Mössbauer sextets 2–4, we calculate individual cation distribution parameters assuming stoichiometry and using only the well-defined A-site Fe^{3+} sextet and equation (3).

All model fits to the XMCD data describing Fe valence and site occupancy are given in supporting information Table S3. Mössbauer fits are given in supporting information Table S4.

3.3.1. Effects of Quenching and Annealing

In general, within-sample variability in the XMCD spectra is smaller than between-sample variability (Figure 6c), but there are no systematic trends with anneal time, anneal temperature, or corresponding ΔT_c . Figure 6a shows a significant and systematic increase in ΔT_c with anneal time for sample b13_35P. By contrast, XMCD-derived Fe site occupancies show no obvious systematic changes (Figure 6b). For comparison, Figure 6d shows calculated spectra for fully ordered ($\epsilon = 1$), fully random ($\epsilon = 0.67$), and intermediate states ($\epsilon = 0.83$). The variability in these modeled spectra suggests that any significant amount of reordering should be resolvable within our data set.

Mössbauer spectra also lack correlation with quench/anneal state for each measured composition (Figure 7 and supporting information Figures S6 and S7). Despite differences in T_c of up to 50 °C, the quenched and annealed absorption spectra are virtually indistinguishable. It seems clear that annealing does not result in any significant intersite exchange of Fe^{2+} and Fe^{3+} ions, as the peak locations, sizes and shapes are almost entirely unaffected. This accords with both the XMCD and M_s results.

3.3.2. Cation Distributions in Pure TMs

We examine here only TMs with no Mg or Al impurities that have not been intentionally oxidized and have not been annealed. While there are no intersite variations in $\text{Fe}^{2+}/\text{Fe}^{3+}$ ordering with anneal time or

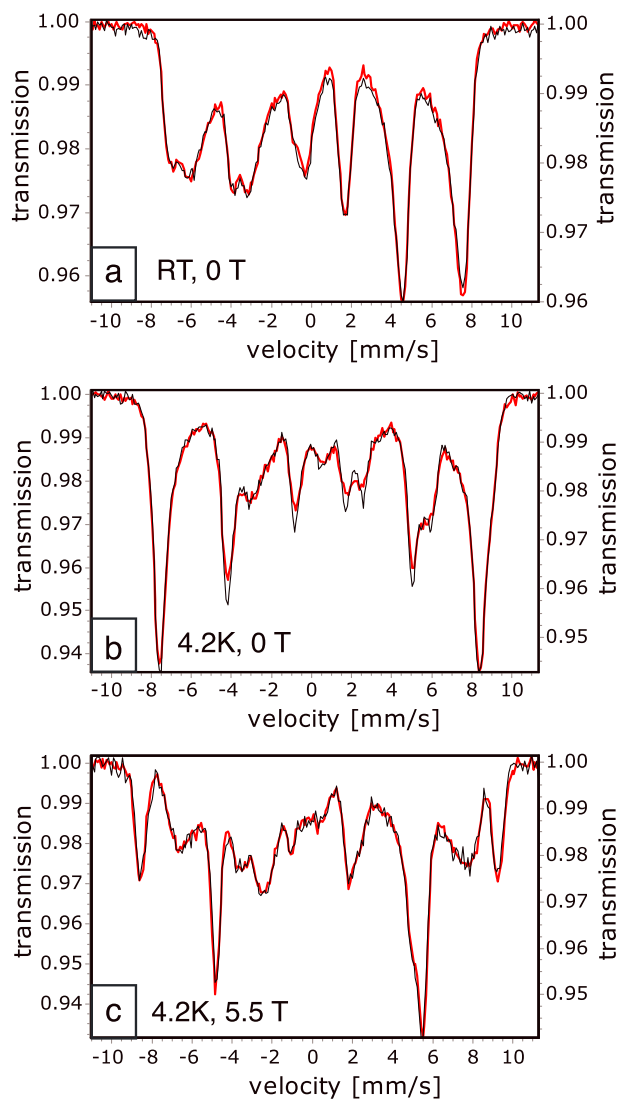


Figure 7. Mössbauer spectra for TM40 sample (b14_40P) after different thermal treatments: (a) room temperature in zero applied field; (b) 4.2 K in zero applied field; (c) 4.2 K in an applied transverse field of 5.5 T. Quenched state spectrum in bold red, referenced to left axis. Spectrum after annealing at 375 °C for 1,000 hr shown by the fine black curve, right axis. Different vertical scales arise primarily from variations in sample mass.

information Figures S8 and S9). This consistent offset might be explained by a surface oxidation that is more apparent in the surface-sensitive XMCD measurements.

3.3.3. TMs Containing Al and Mg

Different cations have different octahedral site preference energy for placement in cubic spinels (Creer & Stephenson, 1972; Henderson et al., 2016; Lavina et al., 2002; Miller, 1959; Navrotsky & Kleppa, 1967). The resulting segregation will depend on the neighboring cations, and it remains incompletely understood in impure TMs.

One composition (TM35) was prepared with a range of Mg^{2+} and Al^{3+} impurity substitutions (from 0 to 0.25 apfu, split evenly between Mg^{2+} and Al^{3+} , $0 \leq [a = b] \leq 0.12$). ZF Mössbauer spectra for TM35 at both 295 and 4.2 K show small and not entirely systematic changes with increasing additional substitution of Al and Mg (supporting information Figure S6). However, in the XMCD data, Mg^{2+} and Al^{3+} appear to be largely accommodated by the octahedral sites (Figure 9), consistent with the $M_s(x', a, b)$ results. The net decrease in Fe^{2+} is almost exactly balanced by the addition of Mg^{2+} . This suggests direct substitution of Mg^{2+} for

temperature at constant composition, we can examine the room temperature cation and vacancy distributions within the TM compositional series. Like the M_s data, XMCD- and Mössbauer-derived cation distributions in pure TMs ($x = 0.33, 0.38, \text{ and } 0.57$) suggest an intermediate degree of order, with some variability between methods.

Our XMCD data are similar to those of Pearce et al. (2010) and demonstrate no significant incorporation of tetrahedral Fe^{2+} for compositions with $x < 0.4$. However, our octahedral fits suggest more Fe^{3+} and less Fe^{2+} (supporting information Figure S8), indicating a degree of nonstoichiometry and vacancies predominantly restricted to the octahedral sites. The degree of nonstoichiometry increases with increasing x , and the calculated number of vacancies per four oxygen increases from ~ 0.05 for $x = 0.33$ to ~ 0.18 for $x = 0.57$ (supporting information Table S3). (For impure TM25, there are no vacancies.) Pearce et al. (2010) also observe slightly increased surface oxidation with increasing x , although to a lesser degree. These vacancy concentrations are high compared to other samples synthesized at high temperatures (e.g., Lattard, 1995), and we assume that it represents a surface oxidation during some part of the sample preparation process or during transfer to the airlock.

Because the A-site Fe^{3+} fits are the most robust for Mössbauer, we calculate the fraction of total iron present as A-site Fe^{3+} and compare distribution models in Figure 8 (see also supporting information Figure S8). To compare with data from other studies, we normalize distribution parameters such that the number of A-site cations is 1 and B-site cations is 2 (Pearce et al., 2010). Our Mössbauer data suggest a cation distribution between the fully disordered model of Akimoto (1954), consistent with Mössbauer results from (Hamdeh et al., 1999). These results are largely independent of any uncertainty in the parameter fitting, depending only on the robustly determined tetrahedral-site ferric sextet and the total absorption area. XMCD data are consistent with a higher percentage of tetrahedral Fe^{3+} , closer to the more ordered models of Néel (1955) and Chevallier et al. (1955). Our XMCD data are very similar to that of Pearce for $x < 0.4$ but diverge at higher x , possibly as a result of the higher number of vacancies. XMCD data from Lilova et al. (2012) reflect a much lower fraction of A-site Fe^{3+} , closer to our own Mössbauer results.

To our knowledge, Lilova et al. (2012) is the only other study to apply both XMCD and Mössbauer techniques to the same set of TMs. In both studies, the amount of tetrahedral Fe^{3+} is consistently lower and tetrahedral Fe^{2+} is consistently higher in the Mössbauer data (Figure 8 and supporting

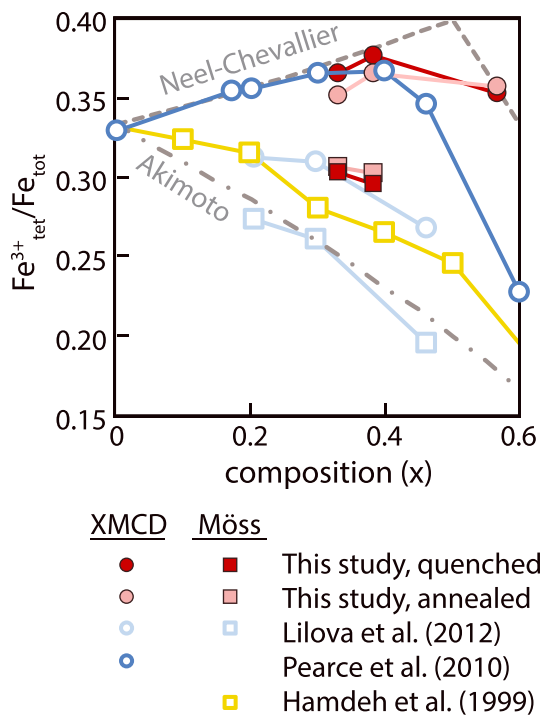


Figure 8. Fraction of Fe as tetrahedral Fe^{3+} , calculated from low-temperature in-field and zero-field Mössbauer spectra and from XMCD. XMCD = X-ray magnetic circular dichroism.

In the ZF spectra, the fourth and fifth absorption peaks are resolved into distinct double peaks, whereas the corresponding unoxidized peaks are less clearly resolved. Overall, however, oxidation produces quite minimal changes in the spectra. The outermost IF peaks, associated with A-site ferric ions, are indistinguishable before and after the oxidation treatment.

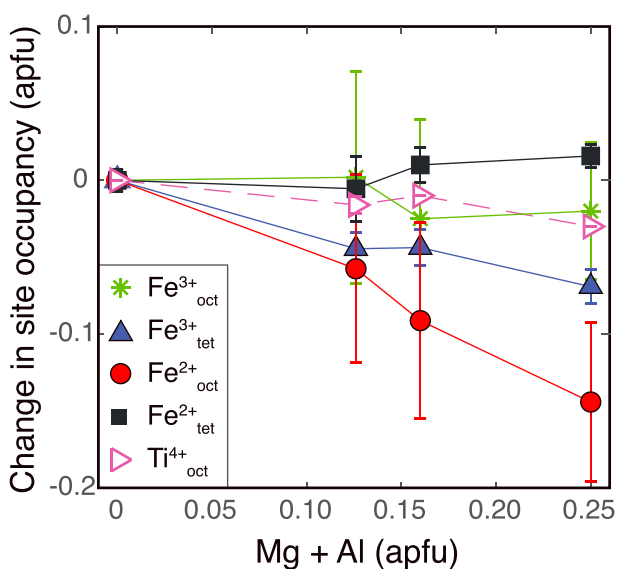


Figure 9. X-ray magnetic circular dichroism changes in cation distribution with increasing Mg^{2+} and Al^{3+} substitution for TM35. Most of the substitution is accommodated in octahedral sites, as demonstrated by the large decrease in $\text{Fe}^{2+}_{\text{oct}}$.

Fe^{2+} and Al^{3+} for Fe^{3+} , with almost all of the Mg^{2+} going into octahedral coordination. The Al^{3+} is roughly split, with slightly more going into tetrahedral coordination. Here, this is accompanied by a small reduction in Ti^{4+} and the movement of some Fe^{2+} from octahedral to tetrahedral.

The Mg *K*-edge XAS data also strongly support the notion that Mg is preferentially in octahedral coordination. The location of the first prominent peak in the near-edge Mg XAS data increases from $\sim 1,309$ eV for tetrahedral coordination to $\sim 1,311$ eV for octahedral coordination (Ildefonse et al., 1995). Further, the relative height of the first two peaks shifts with increasing coordination from a more prominent first peak to a more prominent second peak (Henderson et al., 2016). Mg XAS data for our samples (Figure S10) show a relatively small less prominent first peak at $\sim 1,311$ eV, consistent with Mg in octahedral coordination. This is true for samples with $(\text{Fe}_{2.58}\text{Ti}_{0.26}\text{Al}_{0.08}\text{Mg}_{0.08}\text{O}_4)$ and without $(\text{Fe}_{2.56}\text{Ti}_{0.28}\text{Al}_{0.00}\text{Mg}_{0.16}\text{O}_4)$ Al substitution.

3.3.4. Effects of Oxidation and Cation Deficiency

Although XMCD was performed on some intentionally oxidized samples, the results were difficult to interpret and are not reported here. Because these samples were ground to a finer grain size prior to oxidation (section 2.2), the resulting increase in surface area to volume ratio made it difficult to expose “fresh” interior material upon the second grinding during XMCD preparation. The results are therefore likely strongly dominated by a surface-only oxidation.

Some very slight differences appear in the Mössbauer spectra after oxidation, relative to the initial state (supporting information Figure S7).

After the oxidized material is annealed at 350°C for 100 hr, the Curie temperature is changed by a large amount ($\Delta T_c = 84^\circ$ for the TM40 sample), but the Mössbauer spectra (supporting information Figure S7) still show insignificant changes, especially for IF measurements. There is some sharpening of the fourth and fifth ZF peaks after annealing, but the cation distribution calculated from the A-site ferric sextet is essentially identical to that before annealing, according to the formulation of Hamdeh et al. (1999), which assumes no cation deficiency. More generally, the area fraction f of the A-site ferric sextet is proportional to the ratio of A-site ferric occupancy (ϵ) to stoichiometry degree R (eq. 6), and it is therefore possible that both ϵ and R have decreased during oxidation and annealing while maintaining constant f .

4. Discussion

Although XMCD and Mössbauer data produce some discrepancies in terms of the precise cation distribution within the TM solid solution series, there is reasonable agreement between the two data sets, as well as M_s , in several key respects. XMCD, XAS, and M_s data all demonstrate that the Mg and Al impurities are predominantly accommodated in octahedral sites. Most importantly, XMCD, Mössbauer, and M_s data all strongly suggest that intersite $\text{Fe}^{2+}/\text{Fe}^{3+}$ exchange plays no role in the annealing-induced changes in T_c . As explained below, we therefore infer that some

type of intrasite short-range reordering is taking place via diffusion, and that this process is enhanced by the presence of cation vacancies.

4.1. No Intersite $\text{Fe}^{2+}/\text{Fe}^{3+}$ Exchange

The Curie temperature of a spinel ferrite is in general a measure of the strength of the ferrimagnetic superexchange coupling (Néel, 1955). In spinel ferrites, including TMs, negative A-B coupling is dominant, and A-A and B-B interactions are much weaker, so much so that they are ignored in Stephenson (1972b) theoretical treatment. In the Mössbauer spectra of spinel ferrites, a significant component of B_{hf} is the “supertransferred” hyperfine field, which, like the related phenomenon of superexchange coupling, involves indirect interaction of two magnetic cations through an interposed anion, and here too A-B interactions are generally dominant (Sawatzky & van der Woude, 1974; Schmidbauer, 1987; van der Woude & Sawatzky, 1971). Thus, one might reasonably expect to see a relationship between T_c and B_{hf} in TMs. However, no such systematic relation is observed: quenched and annealed samples of the same composition have Curie temperatures that may differ by 100° or more, but their Mössbauer spectra are indistinguishable. Similarly, there is no systematic relationship between XMCD Fe distribution parameters and anneal time, anneal temperature, or T_c . We have also noted in natural TMs (Bowles et al., 2013; Jackson & Bowles, 2018) that even when the annealed and quenched states have large ΔT_c , they have relatively insignificant changes in M_S and only minor changes in their Mössbauer spectra. Thus, it seems that the changes in Curie temperature cannot be due to significant changes in the intersite ferrous-ferric site occupancy, and that some form of intrasite nanoscale chemical unmixing or clustering may be involved.

4.2. Fine-Scale Chemical Heterogeneity

In low-Ti TMs ($x < 0.25$), room- T Mössbauer spectra are generally found to contain three sextets (Hamdeh et al., 1999; Jensen & Shive, 1973; Sorescu et al., 2012; Tanaka & Kono, 1987). Two of these correspond to the sextets of pure magnetite, representing (1) A-site Fe^{3+} (IS = 0.3 mm/s, QS = -0.02 , $B_{\text{HF}} = 49$ T, $A = 33.3\%$) and (2) B-site $\text{Fe}^{2.5+}$ (IS = 0.67, QS = 0, $B_{\text{HF}} = 46$ T, $A = 66.6\%$). The third sextet is related to the ferrous-ferric imbalance in electron hopping with increasing Ti (Hamdeh et al., 1999; Jensen & Shive, 1973). This so-called C sextet has an IS that is intermediate between that of $\text{Fe}^{2.5+}$ and Fe^{2+} , corresponding to an average oxidation state of approximately $\text{Fe}^{2.3+}$. This observation led Jensen and Shive (1973) to suggest that Ti is nonuniformly distributed within the B sublattice; electron hopping in local cation populations with ferrous/ferric ratios greater than 1 (i.e., in clusters of higher Ti concentration) would result in average oxidation states less than 2.5. The room temperature spectra for low-Ti TMs could thus be explained as the superposition of contributions from higher-Ti clusters (e.g., TM50) and from a relatively pure magnetite matrix. This interpretation has been challenged by Tanaka and Kono (1987). Nevertheless, short-range chemical ordering of octahedral cations has also been suggested on the basis of other evidence, including diffuse scattering in neutron diffraction patterns (Wechsler et al., 1984) and atomistic modeling of the magnesioferrite-qandilite ($\text{MgFe}_2\text{O}_4\text{-Mg}_2\text{TiO}_4$) solid solution, an analogue of the TMs (Harrison et al., 2013).

Our low- T spectra may suggest Ti clustering in another way. The hyperfine field is sensitive to the proportions of magnetic and nonmagnetic nearest neighbors, due to supertransferred B_{hf} , produced at each ion site by the magnetic moments of neighboring cations (van der Woude & Sawatzky, 1971). Each A-site cation has 12 B-site nearest neighbors. If the Ti ions are randomly located within the B sites, the numbers of magnetic and nonmagnetic nearest neighbors for an A-site cation follow the binomial distribution (e.g., Sawatzky et al., 1969). For TM35, the most common situation for an A-site cation is to have four Ti ions among its 12 nearest B-site neighbors, and almost all (93%) of the A cations have between two and seven B-site Ti nearest neighbors. Thus, for randomly distributed Ti, we might expect to see the A sextet both reduced in B_{hf} and broadened relative to that in magnetite, where all of the neighbors of the A-site cations are B-site Fe. This effect was observed by Schmidbauer (1987) in homogeneous cation-deficient ulvöspinel at 5 K; he estimated a decrease in tetrahedral-site B_{hf} of 0.7 T for each neighboring octahedral iron atom replaced by Ti or a vacancy. This is similar to the estimate of 0.8 T per nonmagnetic nearest neighbor by van der Woude and Sawatzky (1971) for various ferrites with random B-site substitutions.

In contrast, if Ti occurs primarily in clusters, we might expect to see distinct A-site sextets, one with a narrow linewidth and B_{hf} comparable to that of pure magnetite and a broader one with significantly lower B_{hf} . This latter distribution seems more consistent with our observations. The very low hyperfine field (~ 21 T) and

broad linewidths (1.2 mm/s) of sextet 4 are comparable to those found by Nakamura and Fuwa (2014) for the octahedral ferrous sextets in stoichiometric ulvöspinel at low temperature (16 K). We infer a chemical heterogeneity that occurs primarily in the octahedral sites, on a scale that is too small to produce two distinct Curie temperatures, but that is clearly detectable by Mössbauer.

This type of nanoscale heterogeneity may be consistent with the observed T_c variations. Mean-field analysis of nanocomposite materials with high- and low- T_c components shows they can exhibit a single T_c which is higher than the volume average of the two components individually and which increases with the spatial scale of the heterogeneity (Skomski & Sellmyer, 2000). Experimental observations of Cu-Ni multilayers (Zheng et al., 1982) show that T_c increases from ~120 to ~500 K as the compositional wavelength increases from ~5 to 25 Å. If some type of chemical clustering or unmixing is taking place during our annealing experiments, the increasing T_c with anneal time may be due to progressive coarsening of the heterogeneity.

Nanoscale chemical clustering, with eventual unmixing, is predicted for the MgFe_2O_4 - Mg_2TiO_4 system by atomistic modeling of cation ordering (Harrison et al., 2013). Henderson et al. (2016) used XMCD and XAS to study Fe ordering in synthetic MgAl_2O_4 - Fe_3O_4 solid solution samples. In the compositional range ~40–90% Fe_3O_4 , they interpret the Fe XAS and XMCD data to represent nanoscale, Fe-rich clusters. One of these samples was also studied by Harrison and Putnis (1995) who found diffuse scattering at the base of XRD diffraction peaks, consistent with short-range cation ordering, or “protonuclei” of potential exsolved phases. Samples of similar composition (Harrison & Putnis, 1996), as well as samples within the FeAl_2O_4 - Fe_3O_4 solid solution (Golla-Schindler et al., 2005), were subsequently found to display thermomagnetic irreversibility of >100 °C ($T_{c\text{-cool}} > T_{c\text{-heat}}$) that was interpreted as chemical exsolution during the $k(T)$ experiment. In both cases exsolution was confirmed by transmission electron microscopy.

A key difference between the above experiments and ours is the temperature of the solvus. In the MgAl_2O_4 - Fe_3O_4 and FeAl_2O_4 - Fe_3O_4 systems, the consolute point of the solvus is relatively high and is not approached during the $k(T)$ experiments. The consolute point in the magnetite-ulvöspinel system is poorly constrained, but is <600 °C (Lilova et al., 2012; Lindsley, 1981; Trestman-Matts et al., 1983), a temperature which is exceeded in all our $k(T)$ experiments. It is therefore conceivable in our case that some of these protonuclei coarsen during annealing at $T < T_{\text{solvus}}$, resulting in higher T_c . The coarsened nuclei then partially or fully rehomogenize during the $k(T)$ run at $T > T_{\text{solvus}}$, lowering T_c and allowing the cycle to be repeated by re-annealing. The longer the anneal time, the coarser the nanoscale clustering becomes and the higher the T_c .

Price (1981a, 1981b) studied the timescales of rehomogenization for naturally exsolved TM ($x \approx 0.38$ and $x \approx 0.47$) with some Mg and Al impurities. He found that exsolution was completely homogenized after ~1 hr at 725 ° and after ~480 hr at 520 °C. If what we observed during our $k(T)$ runs is a rehomogenization, then it is happening at considerably faster timescales; samples spend ~17 min at $T > 500$ °C. However, Price's samples started out with a well-developed, relatively coarse exsolution “cloth” texture, visible under an optical microscope. This was not observed in any samples we studied under microscope. By contrast, the spatial scale of the protonuclei described by Henderson et al. (2016) is estimated to be <100 Å. Even when coarsened, they likely retain wavelengths far short of the well-developed texture observed by Price (1981a). These smaller features would presumably homogenize at shorter time scales.

The observed increase in ΔT_c after intentional sample oxidation is also consistent with this clustering model in that higher vacancy concentrations produce higher rates of cation diffusion (e.g., Aggarwal & Dieckmann, 2002; Van Orman & Crispin, 2010). Faster diffusion would allow the clustering or unmixing process to proceed more rapidly, resulting in a faster change in T_c . Although the fits are poor, the change in ΔT_c vs. \log_{10} time (slope in Figure 3b) is greater for the oxidized sample (b11_30MMn) than for its unoxidized companion. The variable and/or non-log linear behavior in T_c vs anneal time (Figure 3b) may reflect specimen-to-specimen variations in stoichiometry. Increased diffusion rates are one possible explanation for the observations, but it remains possible that the presence of vacancies affects ΔT_c in some other way.

A vacancy-enhanced coarsening and rehomogenization of nanoscale clusters explains much of the data, but there are a number of observations that remain difficult to explain. First, if the Mössbauer results do show evidence of nanoscale B-site chemical heterogeneity, there is still no indication of any difference between the annealed, high- T_c state and the quenched, low- T_c state. Second, although there is a clear enhancement in ΔT_c after intentional oxidation, in the unoxidized samples there is no clear relationship between vacancy

concentration (as calculated by XMCD) and ΔT_c . In fact, the most cation deficient samples (TM50 and TM60) have the smallest ΔT_c . It is possible that the decrease in ΔT_c is related to the increase in Ti, rather than the increase in vacancies. We see a somewhat similar effect in natural samples, where the sample with the highest inferred Ti content (~0.62) has a dramatically smaller ΔT_c (Figure 8 of Jackson & Bowles, 2018). However, natural samples with only slightly less Ti behave similar to other samples, and these compositions ($0.5 < x < 0.6$) are well under any model of the TM solvus. Third, observations of natural samples (Jackson & Bowles, 2018) show that over a wide compositional range ($0.25 < x < 0.6$), the amount of apparent reordering does not vary with distance below the solvus, as would be expected for chemical unmixing. Additionally, it appears that T_c can be driven by annealing to an upper limit of ~500–525 °C, independent of Ti composition within the range $0.2 \leq x \leq 0.5$. This temperature is roughly equivalent to the temperature range over which all samples appear to disorder or homogenize (425–525 °C), suggesting that coupling between magnetic and chemical ordering (as argued by Harrison & Putnis, 1999a; Harrison et al., 2013; Harrison & Putnis, 1997) may play a critical role in the phenomenon.

Ultimately, the system is sufficiently complex and with enough unknowns that the model of vacancy-enhanced chemical clustering best explains the currently available data. Factors that remain incompletely known include the precise shape and position of the solvus, especially when Mg and Al impurities are present; diffusion kinetics at subsolvus temperatures as a function of vacancy concentration, temperature, and position with respect to the solvus, and the possible interplay between magnetic and cation or other ordering.

5. Conclusions

In an effort to better understand the atomic-scale processes underlying previously documented time and temperature-induced changes in T_c in natural TMs, we synthesized a suite of synthetic TMs with a range of Ti, Mg, and Al substitution. XMCD and Mössbauer results suggest that the samples are increasingly non-stoichiometric with increasing Ti content and that the vacancies are dominantly on the octahedral sites. XMCD, XAS, and M_s suggest that Mg substitution is almost entirely accommodated in octahedral sites, while Al substitution is split between the two sites.

Contrary to previous speculations, Mg and/or Al substitution is not required to produce the annealing induced changes in T_c . Pure and impure TMs behave in a similar manner. Additionally, the changes in T_c are enhanced in all synthetic samples by oxidation at low temperature (150 °C).

M_s , XMCD, and Mössbauer results all demonstrate that there is no intersite $\text{Fe}^{2+}/\text{Fe}^{3+}$ reordering associated with the annealing-induced changes in T_c . The data can be best explained by a vacancy-enhanced intrasite (octahedral) nanoscale chemical clustering. This interpretation is supported by Mössbauer data, which display a broadening consistent with Ti clustering. When annealed under the solvus, these nanoscale clusters coarsen, resulting in an increase in T_c . Samples that are intentionally oxidized produce larger changes in T_c with anneal time, suggesting that the diffusion process associated with the coarsening chemical clusters is accelerated by increased cation vacancies.

References

- Aggarwal, S., & Dieckmann, R. (2002). Point defects and cation tracer diffusion in $(\text{Ti}_x\text{Fe}_{1-x})_3\text{O}_4$. II. Cation tracer diffusion. *Physics and Chemistry of Minerals*, 29(10), 707–718. <https://doi.org/10.1007/s00269-002-0284-0>
- Akimoto, S. (1954). Thermo-magnetic study of ferromagnetic minerals contained in igneous rocks. *Journal of Geomagnetism and Geoelectricity*, 6(1), 1–14. <https://doi.org/10.5636/jgg.6.1>
- Arenholz, E., & Prestemon, S. O. (2005). Design and performance of an eight-pole resistive magnet for soft X-ray magnetic dichroism measurements. *Review of Scientific Instruments*, 76(8), 083908. <https://doi.org/10.1063/1.2008027>
- Armstrong, J. T. (1988). Quantitative analysis of silicate and oxide materials: Comparison of Monte Carlo, ZAF, and Phi-Rho-Z procedures. In D. E. Newbury (Ed.), *Microbeam Analysis* (pp. 239–246). San Francisco, CA: San Francisco Press.
- Bowles, J. A., Gee, J. S., Jackson, M., & Avery, M. S. (2015). Geomagnetic paleointensity in historical pyroclastic density currents: Testing the effects of emplacement temperature and postemplacement alteration. *Geochemistry, Geophysics, Geosystems*, 16, 1–20. <https://doi.org/10.1002/2015GC005910>
- Bowles, J. A., & Jackson, M. J. (2016). Effects of titanomagnetite reordering processes on thermal demagnetization and paleointensity experiments. *Geochemistry, Geophysics, Geosystems*, 17, 4848–4858. <https://doi.org/10.1002/2016GC006607>
- Bowles, J. A., Jackson, M. J., Berquó, T. S., Sølheid, P. A., & Gee, J. S. (2013). Inferred time- and temperature-dependent cation ordering in natural titanomagnetites. *Nature Communications*, 4, 1–9. <https://doi.org/10.1038/ncomms2938>

Acknowledgments

We thank Richard Pattrick and Carolyn Pearce for advice and assistance with our initial XMCD studies, and David Keavney for beamline support and advice at APS. We thank Bruce Moskowitz and Peat Sølheid for helpful discussions on Mössbauer analysis, Lindsay McHenry for assistance with XRD measurements, and John Fournelle for microprobe preparation and measurements. Many thanks to reviewers Richard Harrison and Dominique Lattard for their thoughtful and helpful comments that improved the manuscript. This research used resources of the Advanced Light Source (ALS) and the Advanced Photon Source (APS). ALS is a U.S. Department of Energy (DOE) Office of Science User Facility under contract DE-AC02-05CH11231. APS is a U.S. DOE Office of Science User Facility operated for the DOE Office of Science by Argonne National Laboratory under contract DE-AC02-06CH11357. This research was made possible by NSF grants EAR1315971 to J. A. B. and EAR1315845 to M. J. J., as well as access to the Institute for Rock Magnetism, which is supported by the NSF Instruments and Facilities program and by the University of Minnesota. This is IRM contribution #1815. Magnetic data associated with this manuscript are available from the Magnetism Information Consortium (MagIC) database at the website (<https://earthref.org/MagIC/doi/10.1029/2019GC008217>).

- Chevallier, R., Bolfa, J., & Mathieu, S. (1955). Titanomagnétites et ilménites ferromagnétiques. *Bulletin du Société Français Mineralogie et Cristallographie*, 78(4), 307–346. <https://doi.org/10.3406/bulmi.1955.5008>
- Church, N., Feinberg, J. M., & Harrison, R. (2011). Low-temperature domain wall pinning in titanomagnetite: Quantitative modeling of multidomain first-order reversal curve diagrams and AC susceptibility. *Geochemistry, Geophysics, Geosystems*, 12, Q07Z27. <https://doi.org/10.1029/2011GC003538>
- Creer, K. M., & Stephenson, A. (1972). Some consequences of aluminum and magnesium impurities in naturally occurring titanomagnetites. *Journal of Geophysical Research*, 77(20), 3698–3710. <https://doi.org/10.1029/JB077i020p03698/pdf>
- Daniels, J. M., & Rosencwaig, A. (1969). Mössbauer spectroscopy of stoichiometric and non-stoichiometric magnetite. *Journal of Physics and Chemistry of Solids*, 30(6), 1561–1571. [https://doi.org/10.1016/0022-3697\(69\)90217-0](https://doi.org/10.1016/0022-3697(69)90217-0)
- Donovan, J. J., Kremser, D., Fournelle, J. H., & Goemann, K. (2015). Probe for EPMA: Acquisition, automation and analysis, version 11. Probe Software Inc., <http://www.probesoftware.com>, Eugene, Oregon.
- Donovan, J. J., & Tingle, T. N. (1996). An improved mean atomic number background correction for quantitative microanalysis. *Journal of the Microscopy Society of America*, 2, 1–7.
- Droop, G. T. R. (1987). A general equation for estimating Fe³⁺ concentrations in ferromagnesian silicates and oxides from microprobe analyses, using stoichiometric criteria. *Mineralogical Magazine*, 51(361), 431–435. <https://doi.org/10.1180/minmag.1987.051.361.10>
- Evans, B. W., Scaillet, B., & Kuehner, S. M. (2006). Experimental determination of coexisting iron–titanium oxides in the systems FeTiAlO, FeTiAlMgO, FeTiAlMnO, and FeTiAlMgMnO at 800 and 900 C, 1–4 kbar, and relatively high oxygen fugacity. *Contributions to Mineralogy and Petrology*, 152(2), 149–167. <https://doi.org/10.1007/s00410-006-0098-z>
- Fabian, K. (2006). Approach to saturation analysis of hysteresis measurements in rock magnetism and evidence for stress dominated magnetic anisotropy in young mid-ocean ridge basalt. *Physics of the Earth and Planetary Interiors*, 154(3–4), 299–307. <https://doi.org/10.1016/j.pepi.2005.06.016>
- Golla-Schindler, U., O'Neill, H. S. C., & Putnis, A. (2005). Direct observation of spinodal decomposition in the magnetite-hercynite system by susceptibility measurements and transmission electron microscopy. *American Mineralogist*, 90(8–9), 1278–1283. <https://doi.org/10.2138/am.2005.1849>
- Gütlich, P., Bill, E., & Trautwein, A. X. (2011). *Mössbauer spectroscopy and transition metal chemistry*. New York, NY: Springer.
- Hamdeh, H. H., Barghout, K., Ho, J. C., Shand, P. M., & Miller, L. L. (1999). A Mossbauer evaluation of cation distribution in titanomagnetites. *Journal of Magnetism and Magnetic Materials*, 191(1–2), 72–78. [https://doi.org/10.1016/S0304-8853\(98\)00340-0](https://doi.org/10.1016/S0304-8853(98)00340-0)
- Harrison, R. J., Palin, E. J., & Perks, N. (2013). A computational model of cation ordering in the magnesioferrite-quandilite (MgFe₂O₄-Mg₂TiO₄) solid solution and its potential application to titanomagnetite (Fe₃O₄-Fe₂TiO₄). *American Mineralogist*, 98(4), 698–708. <https://doi.org/10.2138/am.2013.4318>
- Harrison, R. J., & Putnis, A. (1995). Magnetic properties of the magnetite-spinel solid solution: Saturation magnetization and cation distributions. *American Mineralogist*, 80(3–4), 213–221. <https://doi.org/10.2138/am-1995-3-402>
- Harrison, R. J., & Putnis, A. (1996). Magnetic properties of the magnetite-spinel solid solution: Curie temperatures, magnetic susceptibilities, and cation ordering. *American Mineralogist*, 81(3–4), 375–384. <https://doi.org/10.2138/am-1996-3-412>
- Harrison, R. J., & Putnis, A. (1997). The coupling between magnetic and cation ordering: A macroscopic approach. *European Journal of Mineralogy*, 9(6), 1115–1130. <https://doi.org/10.1127/ejm/9/6/1115>
- Harrison, R. J., & Putnis, A. (1999a). The magnetic properties and crystal chemistry of oxide spinel solid solutions. *Surveys in Geophysics*, 19(6), 461–520.
- Harrison, R. J., & Putnis, A. (1999b). Determination of the mechanism of cation ordering in magnesioferrite (MgFe₂O₄) from the time- and temperature-dependence of magnetic susceptibility. *Physics and Chemistry of Minerals*, 26(4), 322–332. <https://doi.org/10.1007/s002690050192>
- Henderson, C. M. B., Pearce, C. I., Charnock, J. M., Harrison, R. J., & Rosso, K. M. (2016). An X-ray magnetic circular dichroism (XMCD) study of Fe ordering in a synthetic MgAl₂O₄-Fe₃O₄ (spinel-magnetite) solid-solution series: Implications for magnetic properties and cation site ordering. *American Mineralogist*, 101(6), 1373–1388. <https://doi.org/10.2138/am-2016-5612>
- Hunt, C. P., Moskowitz, B. M., & Banerjee, S. K. (1995). Magnetic properties of rocks and minerals. In T. J. Ahrens (Ed.), *Rock physics and phase relations: A handbook of physical constants* (pp. 189–204). Washington, DC: American Geophysical Union.
- Ildefonse, P., Calas, G., Flank, A. M., & Lagarde, P. (1995). Low Z elements (Mg, Al, and Si) K-edge X-ray absorption spectroscopy in minerals and disordered systems. *Nuclear Instruments and Methods in Physics Research Section B: Beam Interactions with Materials and Atoms*, 97(1–4), 172–175. [https://doi.org/10.1016/0168-583X\(94\)00710-1](https://doi.org/10.1016/0168-583X(94)00710-1)
- Jackson, M., & Solheid, P. (2010). On the quantitative analysis and evaluation of magnetic hysteresis data. *Geochemistry, Geophysics, Geosystems*, 11, Q04Z15. <https://doi.org/10.1029/2009GC002932>
- Jackson, M. J., & Bowles, J. A. (2014). Curie temperatures of titanomagnetite in ignimbrites: Effects of emplacement temperatures, cooling rates, exsolution and cation ordering. *Geochemistry, Geophysics, Geosystems*, 15, 4343–4368. <https://doi.org/10.1002/2014GC005527>
- Jackson, M. J., & Bowles, J. A. (2018). Malleable Curie temperatures of natural titanomagnetites: Occurrences, modes, and mechanisms. *JOURNAL OF GEOPHYSICAL RESEARCH: SOLID EARTH*, 123, 1–20. <https://doi.org/10.1002/2017JB015193>
- Jensen, S. D., & Shive, P. N. (1973). Cation distribution in sintered titanomagnetites. *Journal of Geophysical Research*, 78(35), 8474–8480. <https://doi.org/10.1029/JB078i035p08474>
- Kakol, Z., Sabol, J., & Honig, J. M. (1991). Cation distribution and magnetic-properties of titanomagnetites Fe_{3-x}Ti_xO₄ (0 ≤ x < 1). *Physical Review B*, 43(1), 649–654. <https://doi.org/10.1103/PhysRevB.43.649>
- Lagarias, J. C., Reeds, J. A., Wright, M. H., & Wright, P. E. (1998). Convergence properties of the Nelder–Mead simplex method in low dimensions. *SIAM Journal on Optimization*, 9(1), 112–147. <https://doi.org/10.1137/S1052623496303470>
- Lappe, S. C. L. L., Bowles, J., Jackson, M., & Keavney, D. (2014). XMCD and magnetic evidence for cation reordering in synthetic Mg- and Al-substituted titanomagnetites. Paper presented at American Geophysical Union Fall Meeting, San Francisco, CA.
- Lattard, D. (1995). Experimental evidence for the exsolution of ilmenite from titaniferous spinel. *American Mineralogist*, 80(9–10), 968–981. <https://doi.org/10.2138/am-1995-9-1013>
- Lattard, D., Engelmann, R., Kontny, A., & Sauerzapf, U. (2006). Curie temperatures of synthetic titanomagnetites in the Fe-Ti-O system: Effects of composition, crystal chemistry, and thermomagnetic methods. *Journal of Geophysical Research*, 111, B12S28. <https://doi.org/10.1029/2006JB004591>
- Lavina, B., Salvulo, G., & Della, G. A. (2002). Cation distribution and structure modelling of spinel solid solutions. *Physics and Chemistry of Minerals*, 29(1), 10–18. <https://doi.org/10.1007/s002690100198>
- Lilova, K. I., Pearce, C. I., Gorski, C., Rosso, K. M., & Navrotsky, A. (2012). Thermodynamics of the magnetite-ulvöspinel (Fe₃O₄-Fe₂TiO₄) solid solution. *American Mineralogist*, 97(8–9), 1330–1338. <https://doi.org/10.2138/am.2012.4076>

- Lindsley, D. H. (1981). Some experiments pertaining to the magnetite-ulvöspinel miscibility gap. *American Mineralogist*, 66(7–8), 759–762.
- Miller, A. (1959). Distribution of cations in spinels. *Journal of Applied Physics*, 30(4), S24–S25. <https://doi.org/10.1063/1.2185913>
- Moskowitz, B. M. (1987). Towards resolving the inconsistencies in characteristic physical properties of synthetic titanomaghemites. *Physics of the Earth and Planetary Interiors*, 46(1–3), 173–183. [https://doi.org/10.1016/0031-9201\(87\)90180-4](https://doi.org/10.1016/0031-9201(87)90180-4)
- Murad, E., & Cashion, J. (2004). *Mössbauer spectroscopy of environmental materials and their industrial utilization*. New York, NY: Springer.
- Nakamura, S., & Fuwa, A. (2014). Local and dynamic Jahn-Teller distortion in ulvöspinel Fe_2TiO_4 . *Hyperfine Interactions*, 226(1–3), 267–274. <https://doi.org/10.1007/s10751-013-0921-7>
- Navrotsky, A., & Kleppa, O. J. (1967). The thermodynamics of cation distributions in simple spinels. *Journal of Inorganic and Nuclear Chemistry*, 29(11), 2701–2714. [https://doi.org/10.1016/0022-1902\(67\)80008-3](https://doi.org/10.1016/0022-1902(67)80008-3)
- Néel, L. (1948). Propriétés magnétiques des ferrites: Ferrimagnétisme et antiferromagnétisme. *Annales de Physique*, 12(3), 137–198. <https://doi.org/10.1051/anphys/194812030137>
- Néel, L. (1955). Some theoretical aspects of rock-magnetism. *Advances in Physics*, 4(14), 191–243. <https://doi.org/10.1080/00018735500101204>
- O'Neill, H. S. C., & Navrotsky, A. (1984). Cation distributions and thermodynamic properties of binary spinel solid solutions. *American Mineralogist*, 69(7–8), 733–753.
- O'Reilly, W. (1984). *Rock and mineral magnetism*. New York, NY: Blackie.
- O'Reilly, W., & Banerjee, S. K. (1965). Cation distribution in titanomagnetites $(1-x)\text{Fe}_3\text{O}_4\cdot x\text{Fe}_2\text{TiO}_4$. *Physics Letters*, 17(3), 237–238. [https://doi.org/10.1016/0031-9163\(65\)90504-4](https://doi.org/10.1016/0031-9163(65)90504-4)
- Patrick, R. A. D., van der Laan, G., Henderson, C. M. B., Kuiper, P., Dudzik, E., & Vaughan, D. J. (2002). Cation site occupancy in spinel ferrites studied by X-ray magnetic circular dichroism: Developing a method for mineralogists. *European Journal of Mineralogy*, 14(6), 1095–1102. <https://doi.org/10.1127/0935-1221/2002/0014-1095>
- Pearce, C. I., Henderson, C. M. B., Patrick, R. A. D., van der Laan, G., & Vaughan, D. J. (2006). Direct determination of cation site occupancies in natural ferrite spinels by L_{2,3} X-ray absorption spectroscopy and X-ray magnetic circular dichroism. *American Mineralogist*, 91(5–6), 880–893. <https://doi.org/10.2138/am.2006.2048>
- Pearce, C. I., Henderson, C. M. B., Telling, N. D., Patrick, R. A. D., Charnock, J. M., Coker, V. S., et al. (2010). Fe site occupancy in magnetite-ulvöspinel solid solutions: A new approach using X-ray magnetic circular dichroism. *American Mineralogist*, 95(4), 425–439. <https://doi.org/10.2138/am.2010.3343>
- Press, W. H., Flannery, B. P., Teukolsky, S., & Vetterling, W. T. (1986). *Numerical recipes: The art of scientific computing*. New York, NY: Cambridge University Press.
- Price, G. D. (1981a). Subsolidus phase-relations in the titanomagnetite solid-solution series. *American Mineralogist*, 66(7–8), 751–758.
- Price, G. D. (1981b). Diffusion in the titanomagnetite solid solution series. *Mineralogical Magazine*, 44(334), 195–200. <https://doi.org/10.1180/minmag.1981.044.334.13>
- Sawatzky, G. A., & van der Woude, F. (1974). Covalency effects in hyperfine interactions. *Le Journal de Physique Colloques*, 35(C6), C6–C47.
- Sawatzky, G. A., van der Woude, F., & Morrish, A. H. (1969). Mössbauer study of several ferrimagnetic spinels. *Physics Review*, 187(2), 747–757. <https://doi.org/10.1103/PhysRev.187.747>
- Schmidbauer, E. (1987). 57 Fe Mössbauer spectroscopy and magnetization of cation-deficient Fe_2TiO_4 and FeCr_2O_4 . Part I: 57 Fe Mössbauer spectroscopy. *Physics and Chemistry of Minerals*, 14(6), 533–541. <https://doi.org/10.1007/BF00308289>
- Shirane, G., Cox, D. E., Takei, W. J., & Ruby, S. L. (1962). A study of the magnetic properties of the $\text{FeTiO}_3\text{-Fe}_2\text{O}_3$ system by neutron diffraction and the Mössbauer effect. *Journal of the Physical Society of Japan*, 17(10), 1598–1611. <https://doi.org/10.1143/JPSJ.17.1598>
- Skomski, R., & Sellmyer, D. J. (2000). Curie temperature of multiphase nanostructures. *Journal of Applied Physics*, 87(9), 4756–4758. <https://doi.org/10.1063/1.373149>
- Sorescu, M., Xu, T., Wise, A., Díaz-Michelena, M., & McHenry, M. E. (2012). Studies on structural, magnetic and thermal properties of $x\text{Fe}_2\text{TiO}_4\cdot(1-x)\text{Fe}_3\text{O}_4$ ($0 \leq x \leq 1$) pseudo-binary System. *Journal of Magnetism and Magnetic Materials*, 324(7), 1453–1462. <https://doi.org/10.1016/j.jmmm.2011.12.012>
- Stephenson, A. (1972a). Spontaneous magnetization curves and curie points of cation deficient titanomagnetites. *Geophysical Journal of the Royal Astronomical Society*, 29(1), 91–101. <https://doi.org/10.1111/j.1365-246X.1972.tb06154.x>
- Stephenson, A. (1972b). Spontaneous magnetization curves and curie points of spinels containing two types of magnetic ion. *Philosophical Magazine*, 25(5), 1213–1232. <https://doi.org/10.1080/14786437208226863>
- Tanaka, H., & Kono, M. (1987). Mössbauer spectra of titanomagnetite. *Journal of Geomagnetism and Geoelectricity*, 39(8), 463–475. <https://doi.org/10.5636/jgg.39.463>
- Trestman-Matts, A., Dorris, S. E., Kumarakrishnan, S., & Mason, T. O. (1983). Thermoelectric determination of cation distributions in $\text{Fe}_3\text{O}_4\text{-Fe}_2\text{TiO}_4$. *Journal of the American Ceramic Society*, 66(12), 829–834. <https://doi.org/10.1111/j.1151-2916.1983.tb10996.x>
- van der Laan, G., & Figueroa, A. I. (2014). X-ray magnetic circular dichroism—A versatile tool to study magnetism. *Coordination Chemistry Reviews*, 277–278, 95–129. <https://dx.doi.org/10.1016/j.ccr.2014.03.018>
- van der Laan, G., & Thole, B. T. (1991). Strong magnetic X-ray dichroism in 2p absorption spectra of 3d transition-metal ions. *Physical Review B*, 43(16), 13,401–13,411. <https://doi.org/10.1103/PhysRevB.43.13401>
- van der Woude, F., & Sawatzky, G. A. (1971). Hyperfine magnetic fields at Fe⁵⁷ nuclei in ferrimagnetic spinels. *Physical Review B*, 4(9), 3159–3165. <https://doi.org/10.1103/PhysRevB.4.3159>
- Van Orman, J. A., & Crispin, K. L. (2010). Diffusion in oxides. *Reviews in Mineralogy and Geochemistry*, 72(1), 757–825. <https://doi.org/10.2138/rmg.2010.72.17>
- Walz, F., Torres, L., Bendimya, K., De Francisco, C., & Kronmüller, H. (1997). Analysis of magnetic after-effect spectra in titanium-doped magnetite. *Physica Status Solidi (a)*, 164(2), 805–820. [https://doi.org/10.1002/1521-396X\(199712\)164:2<805::AID-PSSA805>3.0.CO;2-N](https://doi.org/10.1002/1521-396X(199712)164:2<805::AID-PSSA805>3.0.CO;2-N)
- Wanamaker, B. J., & Moskowitz, B. M. (1994). Effect of nonstoichiometry on the magnetic and electrical properties of synthetic single-crystal $\text{Fe}_{2.4}\text{Ti}_{0.6}\text{O}_4$. *Geophysical Research Letters*, 21(11), 983–986. <https://doi.org/10.1029/94GL00877>
- Wechsler, B. A., Lindsley, D. H., & Prewitt, C. T. (1984). Crystal-structure and cation distribution in titanomagnetites ($\text{Fe}_{3-x}\text{Ti}_x\text{O}_4$). *American Mineralogist*, 69(7–8), 754–770.
- Young, A. T., Feng, J., Arenholz, E., Padmore, H. A., Henderson, T., Marks, S., et al. (2001). First commissioning results for the elliptically polarizing undulator beamline at the advanced light source. *Nuclear Instruments and Methods in Physics Research Section A: Accelerators, Spectrometers, Detectors and Associated Equipment*, 467, 549–552.
- Zheng, J. Q., Ketterson, J. B., Falco, C. M., & Schuller, I. K. (1982). The magnetization and Curie temperature of compositionally modulated Cu/Ni films. *Journal of Applied Physics*, 53(4), 3150–3155. <https://doi.org/10.1063/1.331012>